

**DETERMINATION OF FLAME CHARACTERISTICS IN
A LOW SWIRL BURNER AT GAS TURBINE
CONDITIONS THROUGH REACTION ZONE IMAGING**

A Dissertation
Presented to
The Academic Faculty

by

Karthik Periagaram

In Partial Fulfillment
of the Requirements for the Degree
Doctor of Philosophy in the
Guggenheim School of Aerospace Engineering

Georgia Institute of Technology
December 2012

TABLE OF CONTENTS

List of Figures	v
List of Tables	vi
List of Symbols	vii
Summary	viii
1 Introduction	1
1.1 Motivation	2
1.2 Literature Review	7
1.2.1 Low Swirl Burner	7
1.2.2 CH PLIF Implementations	8
1.3 Objectives	10
2 Background	11
2.1 LSB Reacting Flow Field	11
2.1.1 Role of swirl and recirculation zones	12
2.1.2 Axial velocity profile and self-similarity	13
2.1.3 Flame stabilization mechanism	14
2.1.4 Effect of Flow Parameters on Flame Characteristics	15
2.1.4.1 Reference Velocity	15
2.1.4.2 Preheat Temperature	19
2.1.4.3 Swirler Vane Angle	19
2.1.4.4 Equivalence Ratio	20
2.1.4.5 Combustor Pressure	20

2.2	CH PLIF Signal Modeling	21
2.2.1	Basic Model	22
2.2.1.1	Absorption Integral Calculation	24
2.2.1.2	Population Distribution	25
2.2.1.3	Solution	26
2.2.2	CH PLIF Process	27
2.2.3	Improved Model	31
2.2.3.1	Absorption Integral Calculation	35
2.2.3.2	Population Distribution	36
2.2.3.3	Solution	37
3	Experimental Methods and Considerations	38
3.1	LSB Configurations	38
3.1.1	Configuration A	39
3.1.1.1	Test Facility	39
3.1.1.2	Low Swirl Burner	42
3.1.2	Configuration B	43
3.1.2.1	Test Facility	43
3.1.2.2	Low Swirl Burner	45
3.2	Diagnostics	46
3.2.1	Laser Doppler Velocimetry	46
3.2.2	CH* Chemiluminescence	49
3.2.2.1	Image Processing	49
3.2.3	CH Planar Laser-Induced Fluorescence	52
3.2.3.1	Imaging System	54
3.2.3.2	Laminar Flame Setup	54
3.2.3.3	Laser Wavelength Calibration	54

4	CH PLIF Signal Modeling and Validation	57
4.1	CH PLIF Preliminary Experiments	57
4.1.1	Excitation Scan	57
4.1.2	Linearity Test	60
4.2	Fluorescence Signal Modeling	62
4.3	Results	70
5	LSB Flame Characteristics	71
5.1	Effect of Reference Velocity	71
5.2	Effect of Preheat Temperature	73
5.3	Effect of Swirler Vane Angle	75
5.4	Effect of Equivalence Ratio	76
5.5	Effect of Combustor Pressure	77
5.6	Flame Structure	78
6	Conclusions	79
A	Seeder Design	80
	References	84

LIST OF FIGURES

2.1	Schematic of a vaned swirler	11
2.2	Location of recirculation zones in the LSB flow field	12
2.3	Schematic of LSB flame stabilization	14
2.4	Borghi Diagram	18
2.5	Transitions in a basic two-level model for fluorescence	22
2.6	CH $B^2\Sigma^- \leftarrow X^2\Pi$ (0,0) R-bandhead absorption lines	28
2.7	Potential curves for electronic energy levels in the CH molecule	30
2.8	Relevant transitions in a CH molecule	32
2.9	Transitions in the improved CH fluorescence model	33
3.1	Schematic of test facility A	40
3.2	Detail schematic of configuration A	42
3.3	Schematic of test facility B	43
3.4	Detail schematic of configuration B	45
3.5	Schematic of the LDV setup	47
3.6	Sample CH* chemiluminescence data	50
3.7	Schematic of the alexandrite laser	52
3.8	Schematic of the laser calibration experiment	55
3.9	Results of the laser calibration experiment	56
4.1	Schematic of the excitation scan experiment	58
A.1	Schematic of the old seeder design	81
A.2	Schematic of the new seeder design	82

LIST OF TABLES

3.1	Swirler Dimensions	39
4.1	Einstein A coefficients	62
4.2	Quenching Cross-sections	63
4.3	Einstein B coefficientsFIXME	65
4.4	Spectroscopic constants	67

LIST OF SYMBOLS

X_f Flame standoff distance

SUMMARY

CHAPTER 1

1

INTRODUCTION

2

The need to reduce pollutant emissions, particularly the oxides of nitrogen, NO_x , is driven by increasing ecological awareness and stringent government regulations. This spurs efforts in the gas turbine industry to seek cleaner, more environment-friendly combustion concepts. Several mechanisms have been identified to explain the production of NO_x in hydrocarbon-air combustion systems. Of these, the thermal NO_x mechanism discovered by Zel'dovich, is a prominent source of NO_x production at the high temperature conditions encountered in typical combustors. The amount of thermal NO_x produced scales exponentially with the adiabatic flame temperature.

Efforts to reduce the flame temperature have led low NO_x gas turbine manufacturers to adopt one of two options—Lean Premixed (LP) operation, or Rich-Quench-Lean (RQL) operation. Of these, ground-based gas turbines used in power generation have tended to favor LP operation as it is conceptually simpler and avoids issues resulting from inhomogeneous mixing of fuel and air. Further, the ultra-lean operating conditions reduce flame temperature and minimize NO_x production.

In practice, 1800 K is considered a limiting value for the flame temperature, ensuring that the thermal NO_x production is constrained to a minimum.^[1] Operating a combustor at such lean conditions results in weaker combustion processes that are highly susceptible to perturbations and results in combustor instabilities or even flame blow off. This highlights the requirement for robust flame stabilization techniques that can sustain combustion at ultra-lean conditions. In their most basic form, flame stabilization techniques work by making the local reactant velocity and the local flame speed equal. In the context of lean flames, the risk is of the slowly propagating flames to be blown off by the high velocity reactant stream. Consequently, flame

stabilization in gas turbine combustion is brought about either by reducing the local
reactant velocity (e.g. by using bluff body flame holders), by boosting the local flame
velocity (e.g. by enhancing product recirculation), or by providing continual ignition
to the flame (e.g. by using pilot flames).

Swirl-stabilized combustion is a widely used flame stabilization technique in gas
turbine applications.[2,3] It primarily functions by inducing recirculation zones in
the flow field that transport heat and radicals from the products into the reactants.
This enhances the flame propagation velocity by increasing reaction rates within the
flame, resulting in robust flame stabilization. However, the recirculation zones are
associated with high peak residence times for hot combustion products and are sites of
thermal NO_x production in the combustor. Nevertheless, swirl-stabilized combustors
are ubiquitously employed today in land-based gas turbines used for power generation.

More recent research[4] on the Low Swirl Burner (LSB) has identified a potential
solution for this problem. The LSB anchors a lifted flame, reducing the need for high
swirl in the flow field. The lifted, V-shaped flame is stabilized by aerodynamic means
which allows for robust operation even at low equivalence ratios. This weakens the
recirculation zones and eliminates pockets of high residence times, resulting in the
potential for significantly reduced NO_x emissions compared to a similar high-swirl
design.

1.1 Motivation

By comparison to atmospheric pressure experiments, high pressure experimental test-
ing of combustion systems is fraught with difficulties. This is reflected in the com-
paratively smaller subset of publications that report experimental results from high
pressure tests. The primary source of these difficulties stems from the need for com-
plicated testing facilities to reach and maintain high pressures. The inherently limited
access afforded by pressure vessels makes intrusive methods of data gathering nearly

impossible. As a result, any need for spatially resolved data other than temperature
and pressure measurements has to be met by optical diagnostics.

In the context of LSB research, these difficulties have confined much of the published experimental results to ambient conditions. The eventual application of this technology in gas turbine engines requires high quality data acquired at high pressure conditions. Ideally, such data will map the velocity field and heat release in the LSB and study their variation with flow conditions. Since the LSB relies on the velocity field to stabilize its flame, its flame characteristics hold information pertinent to both the velocity field and the heat release distribution within the combustor. This allows a passive diagnostic such as recording the flame chemiluminescence to be used even at high pressure conditions to observe and record usable data about the LSB flame characteristics. Such data, acquired at conditions closer to real world gas turbine combustor operating conditions is of particular interest to the gas turbine industry as it can be used for designing better, more robust combustors with low NO_x emissions.

The primary flame characteristic of interest is the flame standoff distance, defined as the distance from the flame stabilization point to the inlet of the LSB. This metric is useful in gauging the stability of the flame and the need for control systems to closely monitor its tendency to flashback or blow-off. The standoff distance also relates to the heat load experienced by the injector and consequently affects how often the mechanical components of the LSB will require to be replaced in operation. Finally, a systemic variation in the location of the flame over a range of flow parameters may indicate potential problems operating the combustor at previously untested conditions.

Quantifying the shape of the flame can complement the information gleaned from the flame standoff measurements. In case of the V-shaped LSB flame, this can be conveniently obtained by measuring the angle of the flame cone. Changes in the flame angle affect the length of the flame, which is a design consideration for sizing LSB

combustors in gas turbines.

The profile of the flame chemiluminescence along the length of the combustion zone is representative of the local heat release at those locations. A uniform heat release profile is preferred so as to avoid thermally stressing the combustor at the hot spots. Further, since NO_x production rates are so strongly dependent on temperature, the heat release profile can help forecast emissions performance issues of the combustor, particularly when augmented by knowledge of the local flow velocity (and hence, residence time). Finally, the heat release map could be incorporated into n - τ models to predict the onset of thermo-acoustic instabilities in the combustor.

The primary goal of this research work is to study the flame characteristics of the LSB, such as its location and shape, as a means to learn more about the combustor operation at high pressure conditions.

In case of lean hydrocarbon flames, the primary sources of flame chemiluminescence are OH^* ($A^2\Sigma^+ \rightarrow X^2\Pi$ bands, 310 nm), CH^* ($A^2\Delta \rightarrow X^2\Pi$ bands, 430 nm, $B^2\Sigma^- \rightarrow X^2\Pi$ bands, 390 nm), C_2^* ($d^3\Pi \rightarrow a^3\Pi$ Swan bands, 470 nm, 550 nm) and the CO_2^* (band continuum, 320–500 nm). Of these, CH^* chemiluminescence has several advantages that make it suitable for this particular study. First, collection of CH^* chemiluminescence is less affected by blackbody radiation from the walls of the combustor, compared to longer wavelength emissions from a species like C_2^* . Its narrow bandwidth allows one to use a bandpass filter to collect signals from only the wavelengths of interest, further minimizing interference from other light sources. Using such a narrow bandpass filter for a broad band emitter like CO_2^* would result in rejecting most of the available signal. CH^* chemiluminescence occurs in the visible wavelengths and does not require expensive UV lenses or imaging systems with high quantum efficiencies in UV to record it—as would be needed to image OH^* chemiluminescence, for instance. In typical LSB operation, where the flame is not expected to operate near extinction, CH^* chemiluminescence can serve as a reliable indicator

of heat release in the combustor. For all these reasons, CH^* chemiluminescence is a
suitable technique to image the LSB flame.

Ultimately, the amount of information that can be gathered by imaging the flame
chemiluminescence is limited by its spatial resolution. Since chemiluminescence imag-
ing is integrated over the line of sight, studying the flame brush or the flame structure
is beyond its capabilities. A planar imaging technique such as Planar Laser-Induced
Fluorescence (PLIF) is better suited for such applications.

In hydrocarbon flames, species accessible to PLIF are generally minor species in
the flame. PLIF studies of hydrocarbon flames have hitherto focused on the hydroxyl,
OH, radical. However, OH is produced in the flame zone and destroyed by relatively
slow three-body reactions, causing it to persist and be transported away from the
flame and into the product zone.[5] As a result, it does not serve as a direct marker of
the flame front. Instead, the location of the flame is inferred from the sharp gradient
in the OH signal as the reactants are converted into products.

The persistence of OH in the products makes OH PLIF somewhat less suited to
studying flames in flows with high product recirculation. In such flows, the presence
of OH in both the reactants and the products weakens the gradient at the flame.
Further, since OH radicals could be transported transverse to the flame, its presence
or absence serves as an unreliable indicator of local flame extinctions. Nevertheless,
researchers have been able to use OH PLIF successfully[6, 7] to study such flames,
particularly when the images are enhanced by nonlinear filtering techniques.[8, 9]

This study utilizes CH PLIF as the flame visualization technique. CH is produced
and destroyed rapidly by fast two-body reactions, confining it to the thin heat release
zone of the flame. This makes it suitable for use as a marker species for the flame
front.[10] CH is formed during the breakup of hydrocarbon fuel molecules[11] and is
also known to play an important role in the production of prompt NO_x . [12] Hence, it
is a minor species of considerable importance to combustion research. This leads us

to the second motivation for this study—to examine the use of CH PLIF as a flame
imaging technique in combustion systems and further, to use it to image and study
the LSB flame.

The use of CH PLIF to study lean hydrocarbon flames has been difficult in the past
due to several issues. First, the concentration of the CH species in hydrocarbon flames
rapidly declines with equivalence ratio, making high quality imaging of the flame front
at lean conditions challenging. Further, the implementation techniques in the past
have suffered from a host of problems ranging from elastic scattering interference
to saturation issues leading to diminished signal-to-noise ratios. However, a recent
implementation by Li et al.[13] has managed to overcome these issues and has been
demonstrated to image moderately lean flames with good fidelity.

Recent studies[14] have indicated that the formyl species HCO is a superior indi-
cator of heat release in hydrocarbon flames when compared to CH or OH. The HCO
LIF signal has been demonstrated to correlate well with the heat release rate, with
little dependence on equivalence ratio or strain rate. The last factor, in particular, has
been shown to quench the CH PLIF signal[15] in highly strained flames, even when
the flame itself is not extinguished. Unfortunately, the signal levels from HCO LIF
are very poor[14, 16] and are unsuitable for single-shot investigation of hydrocarbon
flames. To overcome this, one study[16] proposed a simultaneous LIF investigation of
formaldehyde, CH_2O , and OH with the reasoning that the formation rate of HCO is
governed directly by the product of the concentration of these two intermediates. This
method has been used in a number of investigations,[17] despite being experimentally
cumbersome. A more recent implementation[18], published after the initiation of
the present effort, has demonstrated single-shot HCO PLIF with moderate signal-to-
noise ratios by utilizing a novel excitation scheme. Follow up studies applying this
technique in other hydrocarbon flames are awaited.

1.2 Literature Review

159

1.2.1 Low Swirl Burner

160

The LSB is a relatively new combustion technology and as such has a brief history. 161
Initial interest in low swirl combustion was primarily motivated by its ability to sta- 162
bilize a freely propagating turbulent flame.[19] As a result, initial designs of the LSB 163
(which at the time used tangential jets to produce swirl) were pursued by Bédard and 164
Cheng[4, 20] as test beds for studying 1-D, planar turbulent flames. Several subse- 165
quent studies[21–27] utilized this behavior and investigated fundamental turbulent 166
flame structure and propagation in the jet LSB. Simultaneously, the discovery of its 167
ability to achieve low NO_x emissions prompted interest in commercial applications of 168
the LSB, such as in industrial furnaces and boilers.[28–30] 169

The current form of the LSB (as used in this thesis) using vanes to generate swirl 170
was originally modified from a typical production swirl injector used in gas turbine 171
combustors. The results of testing this new design were published by Johnson et 172
al.[31] The design elements of the new injector—now called the Low Swirl Injector 173
(LSI)—were tuned in an atmospheric pressure test rig using LBO and flame location 174
as the criteria. The atmospheric tests were conducted with preheated reactants at 175
up to 650 K. The more interesting results from the work came from high pressure, 176
high preheat tests (15 atm, 700 K) in a test rig with limited optical access. The 177
researchers measured a dramatic (50%) reduction in the NO_x emissions by switching 178
from the original (“High” Swirl Injector) to the new low swirl design. The emissions 179
performance was also noted by Nazeer et al.[32] 180

Subsequent studies by Cheng et al.[33,34] explored the characteristic velocity field 181
in the LSB using PIV and discovered self-similar behavior that implied that the flame 182
location was unaffected by the mass flow rate of the reactants. This led to further 183
insights into the flame stabilization mechanism used by the LSB. These results will 184

be revisited in Chapter 2 in greater detail.

The effects of using an enclosure to contain the combustion zone were explored by Cheng et al.[35] who found scaling criteria for minimizing the effect of the enclosure on the flame stabilization location. More recent work has tended to focus on the use of various fuels such as hydrogen mixtures[36] with and without dilution[37], landfill gas[34, 38] and syngas[39].

Relatively little research has focused on the flame location and other characteristics and studied their variation at gas turbine relevant conditions. Notably, Petersson et al.[40] used a different modified version of the LSB that had fewer vanes compared to the one tested by Cheng and co-workers, and used a bevy of techniques to study the turbulent flame. Although their test conditions and burner geometry were different, their results were consistent with other results published by Cheng et al. Of particular interest to this discussion are their OH PLIF images of a non-preheated, atmospheric flame at low flow rates. Using these images, they extracted mean reaction progress variable contours for the flame. While their motivation was to develop a detailed database to compare and validate LES models, it remains one of the few works that affords us a look at the structure of the LSB flame with good spatial resolution.

1.2.2 CH PLIF Implementations

Historically, CH was the first species to be detected using LIF in a flame.[41] Early attempts[42, 43] to excite the CH layer used variations of short-pulsed, YAG-pumped dye laser output targeting transitions in one branch of the $A^2\Delta \leftarrow X^2\Pi$ (0,0) band and observing resulting fluorescence in the same band, but at a different rotational branch. These methods relied on the strong absorption of the $A-X$ bands to generate high signal values, but suffered from interference from elastic scattering. Further, the short pulsewidth and narrow spectral bandwidths of the excitation sources quickly saturated the transition being pumped, limiting the amount of LIF signal measured.

Namazian et al.[44] and Schefer et al.[45] had better success at overcoming interference issues by exciting the $A - X$ (0,0) band, but observing fluorescence from the (0,1) band. Another similarly non-resonant technique was proposed by Paul et al.[46] who excited the $A^2\Delta \leftarrow X^2\Pi$ (1,0) band and observed resulting fluorescence from the (1,1) and (0,0) bands. These approaches provide good separation between the excitation and emission wavelengths, but are hampered by the spectroscopic properties of the CH system—which will be explored further in Section 2.2.2—which disfavor radiative transitions in the non-diagonal (0,1) or (1,0) bands. Further, Namazian et al.’s scheme suffers from interference due to Raman scattering of the excitation beam by the fuel species, which overlaps the (0,1) band fluorescence.

Carter and several others[47–55] pumped the $B^2\Sigma^- \leftarrow X^2\Pi$ (0,0) band and utilized fast electronic transfer from the $B^2\Sigma^-$, $v = 0$ to populate the $A^2\Delta$, $v = 0, 1$ levels. This way, they could observe the strong emission from $A^2\Delta \rightarrow X^2\Pi$ (1,1) and (0,0) bands. This method overcame the interference issues by providing sufficient spacing between the excitation and emission wavelengths, but suffered from saturation issues due to the short pulsewidth of the excitation sources. Further, at high laser irradiance, the group recorded noticeable interference from fuel LIF.

Li et al.[13, 56, 57] investigated the use of an alexandrite laser[58] to improve upon the previous excitation scheme by targeting the R-bandhead of the $B^2\Sigma^- \leftarrow X^2\Pi$ (0,0) transition with an excitation beam having a much longer pulse duration than Nd:YAG pumped dye lasers. This excitation scheme offers several advantages over previous implementations. First, it inherits the large spacing between the excitation and emission wavelengths and reduced interference issues from Carter et al.’s implementation. Next, by using a long pulsed laser beam, it overcomes saturation issues. In fact, the researchers note that the pulsewidth is long enough to allow the same CH molecule to go through the excitation-deexcitation sequence several times, boosting signal output. This aspect of the implementation is further enhanced if the laser is

operated in multimode, with a large spectral bandwidth, allowing the laser to tar- 238
get several lines near the R-bandhead. The resultant improvement in signal-to-noise 239
makes this technique suitable to study even low equivalence ratio hydrocarbon flames. 240
This is the excitation scheme that is used in this study. 241

1.3 Objectives 242

2.1 LSB Reacting Flow Field

This section will discuss the salient features of the LSB flow field that will play an important part in the discussions to follow in this thesis.

As discussed in Section 1.2.1, there have been multiple variations of the LSB design used by researchers in the past. Broadly, they can be classified into jet-LSB and vane-LSB, based on the means used to produce the weak swirl in the flow field. This study reports findings relating to the vane-LSB design, and hence, our discussion will also pertain to the vane-LSB.

The vane-LSB—or simply *LSB* from here on—uses a vaned swirler with a central open section. A typical design of such a swirler is shown in Figure 2.1. The swirler splits the flow into two streams, imparting swirl only to the outer annular flow. A perforated plate covers the open central section of the swirler and controls the relative mass flow split between the central unswirled flow and the annular swirling flow. The

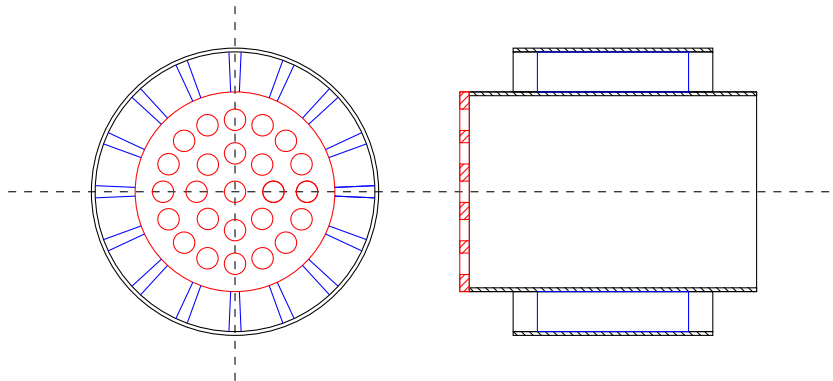


Figure 2.1: The figure shows a top and side cross-sectional view of the vaned swirler design used in this study. The perforated plate used to control the relative mass flow split is highlighted in red, while the vanes used to generate swirl are highlighted in blue.

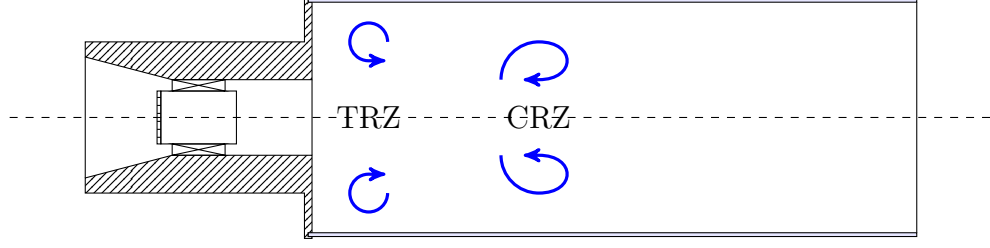


Figure 2.2: The figure shows the locations of the recirculation zones in the LSB flow field. The Toroidal Recirculation Zone (TRZ) forms near the abrupt area expansion. The Central Recirculation Zone (CRZ) forms within a recirculation bubble along the centerline of the combustor.

swirler is located at the head of a constant area nozzle which abruptly expands into the combustion zone.

2.1.1 Role of swirl and recirculation zones

The amount of swirl present in the resulting flow is characterized by a theoretical swirl number, S , which represents the ratio of angular momentum to axial momentum in the flow field. Cheng et al.[29] and later, Littlejohn et al.[30] reduced this to the following equation.

$$S = \frac{2}{3} \tan \alpha \frac{1 - R^3}{1 - R^2 + \left[M^2 \left(\frac{1}{R^2} - 1 \right)^2 \right] R^2} \quad (2.1)$$

In Equation 2.1, R is the ratio of the diameter of the central section to the outer diameter of the swirler. Similarly, M is the ratio of the mass flow rate through the central portion to the mass flow rate through the outer (vaned) portion of the swirler. Finally, α is the angle of the vanes of the swirler.

Along with the recess length of the swirler, the theoretical swirl number was identified to be a key parameter that determines the LSB operating regime.[30] Typical values of S in low swirl combustion range from 0.4–0.6.

Figure 2.2 shows the locations of the notable recirculation zones in the LSB flow field. The toroidal recirculation zone forms near the inlet, while the central recircu-

lation zone forms within a recirculation bubble along the centerline. In conventional swirl combustion, the function of the swirl is to induce these recirculation zones that help stabilize the flame by causing a feedback of heat and radicals from the products into the reactants. In particular, the toroidal recirculation zone traps hot combustion products and continually ignites the reactants at the base of the flame.[31]

In the LSB flow field, these recirculation zones are not only much weaker, but also, do not play any part in the stabilization of the flame. Instead, the LSB flame is a freely propagating turbulent flame that is stabilized by the divergent flow coming from the inlet nozzle. The function of the swirl in the LSB flow field is merely to enhance this divergence. This purely aerodynamic means of stabilizing the flame differentiates the LSB regime from conventional swirl combustion.

2.1.2 Axial velocity profile and self-similarity

The mean axial velocity profile along the centerline of the LSB exhibits a characteristic linear profile in the near field of the inlet. Two features can be associated with this profile. First, extrapolating the velocity profile to the point upstream where the axial velocity equals the reference velocity, we obtain the location of the virtual origin. The virtual origin represents the point upstream where the divergence seemingly originates from. Second, we can measure the slope of the linear region of the axial velocity profile and obtain the axial stretch rate.

Cheng et al.[33,34] investigated these two parameters using a non-preheated setup at atmospheric pressure. They found that the virtual origin for reacting LSB flow fields asymptotically decreases at low/moderate Reynolds numbers, while the mean axial stretch rate is nearly independent of the same parameter. This means that at moderately increasing Reynolds numbers, the divergent flow structure shifts upstream into the injector, eventually ceasing this motion for high Reynolds number values (above 70,000).

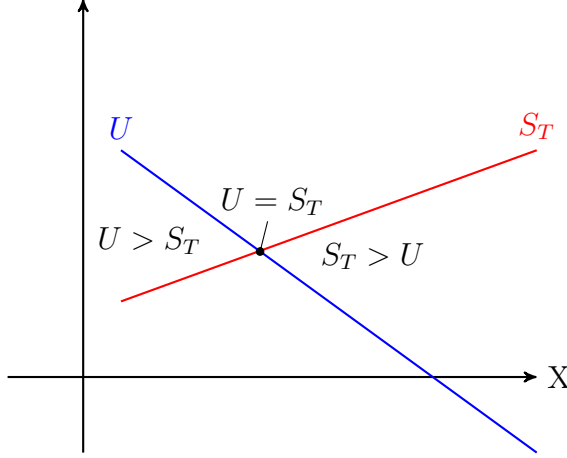


Figure 2.3: The figure above illustrates the robustness of the LSB flame stabilization mechanism. The flame is stabilized at the point where the reactant velocity, U , and the turbulent flame speed, S_T , are equal. Perturbations to the flame standoff distance to the left or the right are counteracted by either U or S_T respectively making this a stable equilibrium.

Since this shift does not affect the slope of the velocity profile, the researchers plotted the mean axial velocity profiles for different operating conditions, shifted to have a common virtual origin. Further, the velocity profiles were normalized by the mass-averaged inlet velocity (called the reference velocity). The resultant plot showed that the linear section of the divergent flow was self-similar at all the velocities tested. This self-similarity of the mean axial velocity profile was used to explain other observations regarding the flame characteristics which we will discuss shortly.

2.1.3 Flame stabilization mechanism

The flame stabilization mechanism in the LSB is purely aerodynamic. The turbulent flame is not anchored in the sense of an attached flame, but freely propagates into the reactants. Conventionally, attached flames are preferred in combustion systems as lifted flames are associated with unstable/undesirable characteristics like blow off. However, the LSB flame is robustly stabilized and not prone to blow off.

The location where the LSB flame is stabilized is marked by the equilibrium condition for flame stabilization—the local reactant velocity, U equals the local turbulent

flame propagation velocity, S_T . The decrease in the local reactant velocity along the centerline of the combustor is accompanied by an increase in the local turbulence level. In other words, along the axis of the combustor, at the location where the flame is stabilized, the reactant velocity is decreasing, while the turbulent flame propagation velocity (which scales with the local turbulence) is increasing.

This sets up a stable equilibrium for the flame as shown in Figure 2.3. Small perturbations causing the flame to move upstream are offset by the increased reactant velocity, while similar perturbations downstream are counteracted by the increased turbulent flame speed. This is the mechanism behind the robust stabilization of the LSB flame.

2.1.4 Effect of Flow Parameters on Flame Characteristics

The operating conditions of the LSB combustor are fully described by four fundamental flow parameters; the combustor pressure, p , the combustor temperature, T , the mixture equivalence ratio, ϕ , and the reference velocity, U_0 . The reference velocity represents the mass-averaged velocity of the reactants entering the LSB and is defined after Cheng et al.[29] as follows.

$$U_0 = \frac{\left(\frac{\dot{m}_{air}}{\rho_{air}}\right) + \left(\frac{\dot{m}_{fuel}}{\rho_{fuel}}\right)}{\frac{\pi d_s^2}{4}} \quad (2.2)$$

In this section, we will discuss the effect each of these flow parameters has on the location and shape of the LSB flame.

2.1.4.1 Reference Velocity

As described earlier in Section 2.1.3, the LSB flame is stabilized where the local reactant velocity and turbulent flame speed are equal.

Unlike the laminar flame speed, S_L , the turbulent flame speed is not uniquely

determined by the reactant composition and thermodynamic conditions. Instead, it is a function of the flow characteristics and the burner geometry as well.

A simple model proposed by Damköhler[1] treats the turbulent flame as a wrinkled laminar flame. The presence of these wrinkles vastly increases the surface area of the flame, increasing the rate at which the reactants can be consumed through the flame. The size of these wrinkles can be related to the rms of the local reactant velocity, u' . Expressed mathematically, this leads to Equation 2.3.

$$\frac{S_T}{S_L} = 1 + \frac{u'}{S_L} \quad (2.3)$$

Cheng et al.[23, 38, 39] observed that the slope of this linear relationship was dependent on the fuel mixture being used. This idea is encapsulated in Equation 2.4 that presents a modified version of Equation 2.3.

$$\frac{S_T}{S_L} = 1 + K \frac{u'}{S_L} \quad (2.4)$$

The constant K has a value of around 1.73 for methane-air mixtures and a somewhat higher value—3.15—for hydrogen-air mixtures,[38] suggesting that the turbulent flame speed is affected strongly by the thermo-diffusive properties of the fuel.

In order to predict the expected effect of increasing the reference velocity, consider the following analysis at the flame standoff location where $U=S_T$.

$$\begin{aligned}
\frac{S_T}{S_L} &= 1 + K \frac{u'}{S_L} \\
S_T &= S_L + K u' \\
\implies U &= S_L + K u' \\
U_0 - \frac{dU}{dx}(X_f - X_0) &= S_L + K u' \\
\therefore X_f &= X_0 + \frac{1 - \left(\frac{S_L}{U_0} + K \frac{u'}{U_0} \right)}{\frac{dU}{dx}} \tag{2.5}
\end{aligned}$$

Consider the terms on the RHS of Equation 2.5. As discussed in Section 2.1.2, the virtual origin location is invariant for moderate to high values of reference velocity. In the same section, we also discussed how the slope of the velocity profile, $\frac{dU}{dx}$, is also invariant with reference velocity. In the numerator of the second term, the local turbulence intensity, $\frac{u'}{U_0}$, can also be expected to be a constant, since u' should scale with the reference velocity in the same manner as long as the burner geometry doesn't change. That leaves only the term $\frac{S_L}{U_0}$ as a function of U_0 . Typically, the laminar flame speeds are an order of magnitude lower ($\approx O(1)$ m/s) than the reference velocities at which the LSBs are operated ($\approx O(10)$ m/s). As a result, this term is vanishingly small, leaving the RHS independent of U_0 . In other words, the flame location, X_f is expected to be invariant with the reference velocity at which the LSB is operated.

Now, consider the effect of increasing the reference velocity on the angle of the flame cone. Again, the stabilization condition is equality between the local velocity and the turbulent flame speed. However, along the flame cone, the reactant velocities are much higher and the flame propagation can only occur at an angle to the reactant velocity. Increasing the reference velocity does not affect any of these factors and thus, the flame angle can also be expected to be unchanged at higher reference velocities.

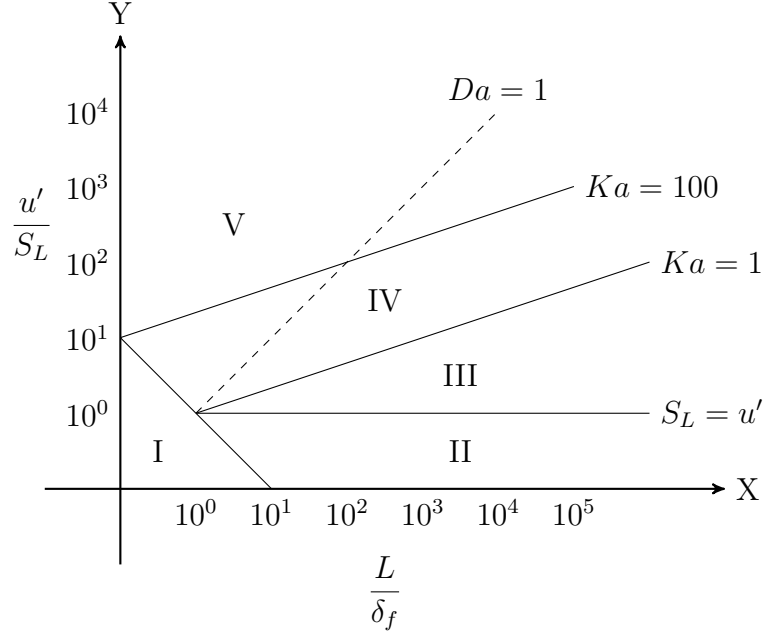


Figure 2.4: The figure shows the Borghi diagram marking the various regimes of premixed turbulent combustion—I. laminar flames, II. wrinkled flamelets, III. corrugated flamelets, IV. thin flame zones, and V. broken reaction zones—separated by contours of Karlovitz number.

Finally, the effect of the reference velocity on the structure of the turbulent flame should be considered. Depending on the characteristics of the flame structure, the operation point can be placed on a Borghi diagram, as shown in Figure 2.4. It is useful to examine the effect of various parameters on the flame structure by examining the tendency of the operating point to shift on the Borghi diagram. To do so, the key parameters to be considered are the rms velocity, u' , the laminar flame speed, S_L , the integral length scale of the flow, L , and the flame thickness, δ_f .

Increasing the reference velocity will be accompanied with a concomitant increase in the level of turbulence in the flow, but changes none of the other parameters. As a result, the operating point will traverse vertically on the Borghi diagram. If the LSB operates in the wrinkled flamelets regime to begin with, at very high reference velocities, it may be expected to cross over into the corrugated flamelets regime. This will be marked by the formation of holes and pockets in the flame sheet.

2.1.4.2 Preheat Temperature

Now, let us consider the effect of increasing the preheat temperature on the flame location, shape and structure. As discussed earlier, the flame standoff distance is decided by the local reactant velocity and the local turbulent flame speed. Increasing the preheat temperature impacts these parameters in two ways. First, the higher temperature increases the kinematic viscosity of the flow. The mechanism that transports the axial momentum in the radial direction and causes the flow to diverge is driven by viscosity. Enhanced viscous effects will result in a steeper decrease in the axial velocity. This also causes an increased production of turbulent kinetic energy. Second, global reaction rates increase with temperature, causing the laminar flame speed to increase. The net result of the increased turbulence and laminar flame speed is that the turbulent flame propagates faster. As a result of this, the flame will be expected to stabilize closer to the inlet of the LSB.

The effect on the flame shape is harder to predict. The increased divergence will drive more axial momentum into the shear layer, increasing the local velocity of the reactants. At the same time, the increased u' and S_L drive up the turbulent flame speed. This may either increase or decrease the angle of the flame.

Finally, we return to the Borghi diagram to consider the effect of a higher preheat temperature on the flame structure. The rapid rise of S_L with temperature will dominate the change in the ordinate of the operating point, causing the operating point to move down. On the X-axis, the flame thickness slightly decreases with temperature, driving the point to the right. The net down-and-right movement of the operating condition drives the flame regime closer to wrinkled flamelets.

2.1.4.3 Swirler Vane Angle

The swirler vane angle directly affects the amount of swirl present in the flow field. Since the LSB utilizes swirl to enhance the divergence of the flow near the inlet,

an increased vane angle will result in a sharper deceleration of the reactants and a more upstream stabilization location of the turbulent flame. This is corroborated by past research[59] which reported shorter, wider (higher flame angle) flames when the amount of swirl in a combustor was increased. Increasing the swirl does not affect any other parameters in the flow and is hence not expected to have a significant effect on the flame structure.

2.1.4.4 Equivalence Ratio

Operating the LSB with a richer fuel-air mixture increases the net heat release in the combustor rapidly. While the velocity flowfield is unaffected by changing the reactant composition (except in response to the heat release), the turbulent flame speed is enhanced. Thus, increasing the equivalence ratio will cause the flame to move upstream and stabilize closer to the inlet. The response of the flame angle to this change is not immediately discernible.

On the Borghi diagram, the increase in S_L and decrease in flame thickness caused by the richer mixture will drive the operating point down and to the right, towards the wrinkled flamelets regime.

2.1.4.5 Combustor Pressure

Finally, the effect of increasing the combustor pressure on the flame characteristics is of much pertinence it is likely to be varied in gas turbine engines to change the loading/power output. Researchers[60, 61] have observed that the effect of the combustor pressure on the turbulent flame speed is minimal, causing a slight drop in the turbulent flame speed at high pressures. Griebel et al.[62] attribute this behavior to the fact that the decrease in S_L with pressure is compensated for by broadening of the turbulence spectrum, resulting in a higher turbulent flame surface area. Higher pressures also decrease the kinematic viscosity of the reactant flow, causes a some-

what less efficient divergence at the inlet of the LSB. The net effect of the two is
expected to cause the flame to stabilize slightly further downstream from the inlet of
the LSB.

This has repercussions for the gas turbine designers as a flame stabilized further
away from the inlet is likelier to be blown off due to perturbations. In practice,
operating at high combustor pressure also causes increased preheat temperatures and
the two effects should counteract each other.

The slight decrease in the turbulent flame speed should cause the flame angle to
decrease by a small amount.

Finally, it is interesting to examine this on a Borghi diagram to deduce any changes
in the flame structure that might result. Kobayashi et al.[63] report that the increas-
ing pressure causes a weak drop in u' , reaching a minimum around 10 atm. This drop,
though, is expected to be dominated by the fall in laminar flame speed with pres-
sure, causing the u'/S_L factor to increase with pressure. On the X-axis, the integral
length scale is very nearly unaffected by the pressure change, but the flame thickness
decreases rapidly. Thus, pressure causes the operating point to move up and to the
right on the diagram. At most, this can cause the turbulent regime to change from
wrinkled laminar flamelets to corrugated flames. In the absence of a drastic change
in the turbulent flame, the only observable effect is likely to be an increase in the fine
structure of the wrinkles in the flame due to the broadened turbulence spectrum.

2.2 CH PLIF Signal Modeling

While the intent and scope of this work is to use CH PLIF as a visualization technique
to image the flame front with high fidelity, it would be extremely useful to be able
to predict the CH PLIF signal intensity for different reactant mixtures and initial
conditions as a means to gauge the feasibility of applying the technique to acquire
high fidelity images of the flame at those conditions. To that end, this discussion

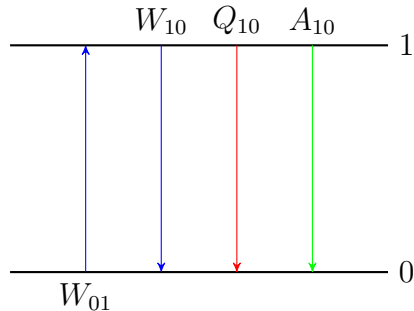


Figure 2.5: The figure shows energy levels and transitions between two levels, labeled 0 and 1, in a basic model of laser-induced fluorescence. Stimulated absorption and emission are shown in *blue*, collisional quenching is shown in *red* and spontaneous emission is shown in *green*.

will attempt to develop a mathematical model to calculate, in a semi-quantitative 460
manner, the rate of CH PLIF photons emitted by the illuminated reaction zone. The 461
following discussion introduces important concepts in LIF signal intensity calculation 462
using a simple two-level model and then proceeds to apply these concepts to model 463
the more complicated physical processes in the CH system. 464

2.2.1 Basic Model 465

In its most basic form, the number of fluorescence photons generated in a system, Φ is 466
the product of the number of emitters, N and the Einstein coefficient for spontaneous 467
emission, A . 468

$$\Phi = N \times A \quad (2.6)$$

The fluorescence photons produced are radiated in all directions and only a frac- 469
tion of these can be recorded by a collection system in an experiment. This fraction 470
is determined by the experimental set up, the collection angle, and the efficiency of 471
the optics and the detector used to record the signal. For this analysis, however, this 472
fraction is omitted to reduce complexity. 473

In a simple two-level model for the fluorescing system, as shown in Figure 2.5, 474

Equation 2.6 may be expanded in terms of the number density of the emitters, n , and the volume in which the fluorescence occurs, V .

$$\Phi = n_1 V A_{10} \quad (2.7)$$

The population of the upper state, n_1 can be solved for by rate analysis. The mathematical treatment is not particularly complicated and is covered in detail by various textbooks and review papers.[64, 65] Here, we shall merely remark that the functional form of the solution has two limiting cases. The limits are decided by the relative magnitudes of the pumping rate, W_{01} , and the relaxation rate given by the sum of the spontaneous emission rate and the collisional quenching rate, $A_{10} + Q_{10}$. The former is the rate at which the upper energy level is populated through absorption. The latter represents the rate at which the molecules return to the lower energy state, either through spontaneous emission or by losing energy to other molecules through inelastic collisions.

When the pumping rate is far lower compared to the relaxation processes ($W_{01} \ll A_{10} + Q_{10}$), the solution tends to the weak excitation limit. In this limit, the functional form of the solution is shown in Equation 2.8

$$\Phi = n_0 V W_{01} \overbrace{\frac{A_{10}}{A_{10} + Q_{10}}}^{\text{Fluorescence Yield}} \quad (2.8)$$

The $n_0 V W_{01}$ term in Equation 2.8 represents the number of molecules that are excited to the upper state per second, while the fluorescence yield represents the fraction of these molecules that will produce a LIF signal. In typical combustion environments, the fluorescence yield is usually small, since the collisional quenching rate dominates the spontaneous emission rate. The rate of collisional quenching of the marker species by another species in the flame is proportional to the frequency of collisions between the two species. Further, the effectiveness of such collisions is

decided by a collision cross-section, σ , which is often a function of the temperature. 497
Equation 2.9 presents the calculation of the collisional quenching rate by summation 498
over all the species, i , in the flame. 499

$$\begin{aligned}
Q_{10} &= \sum_i n_i \times \sigma_i \times c_i \\
&= \sum_i n_i \sigma_i \sqrt{\frac{8kT}{\pi \mu_i}} \\
&= \sqrt{\frac{8kT}{\pi}} \sum_i \frac{n_i \sigma_i}{\sqrt{\mu_i}}
\end{aligned} \tag{2.9}$$

In Equation 2.9, k is the Boltzmann constant, T is the local temperature, n_i is 500
the number density of species i and μ_i represents the reduced mass of the colliding 501
molecules, given by Equation 2.10. 502

$$\mu_i = \frac{m_i m}{m_i + m} \tag{2.10}$$

In Equation 2.10, m is the mass of the marker species, while m_i are the masses 503
of the colliding species. Since LIF in combustion primarily targets minor species, by 504
probability, these collisions will almost always occur with major species in the system. 505
As a result, the summation in Equation 2.9 need only be carried out over the major 506
species in the flame. The values of the local number densities of the major species can 507
be measured by techniques like Raman scattering, or can be obtained from solving 508
chemical kinetics models. 509

2.2.1.1 Absorption Integral Calculation 510

Let us now briefly examine the first term in Equation 2.8 in further detail. Let $\phi(\nu)$ 511
represent the normalized lineshape of the absorption line being excited, such that 512
 $\int \phi(\nu) d\nu = 1$. If B_{01} is the Einstein coefficient for absorption for the line being 513

excited, the term $B_{01}\phi(\nu)$ represents the spectral absorptivity of the line at ν . B_{01} is usually presented in m^2/Js for LIF applications. Similarly, let I_ν be the spectral intensity of the incident radiation, which is the intensity (power per area) of the laser beam per spectral interval. Let $\psi(\nu)$ be the normalized spectral profile of the laser lineshape, such that $I_\nu = I\psi(\nu)$ and $\int \psi(\nu)d\nu = 1$. I_ν is usually given in $\text{W}/\text{cm}^2/\text{cm}^{-1}$ for ease of use in laser applications.

The product of the spectral absorptivity and the spectral intensity integrated over the spectrum, gives the pumping rate, W_{01} , as shown in Equation 2.11. The factor c is the speed of light, which brings the units of W_{01} to s^{-1} .

$$W_{01} = \frac{I}{c} \int \psi(\nu) B_{01} \phi(\nu) d\nu \quad (2.11)$$

2.2.1.2 Population Distribution

Once again, consider Equation 2.8, this time focusing on the term n_0 , the number density of the marker species in the lower energy state that are available for excitation to the upper state. In reality, this comprises only a small subset of all the available molecules of the marker species in the system.

$$n_0 = n f_0 \quad (2.12)$$

In Equation 2.12, n is the number density of all marker species over all the energy levels, while the fraction, f_0 , represents the proportion of the marker species that populates the lower energy level.

2.2.1.3 Solution

Substituting Equations 2.11 and 2.12 into 2.8, and noting that the signal produced is actually integrated over a volume,

$$\Phi = \int_V \frac{nA_{10}}{A_{10} + Q_{10}} \frac{I}{c} f_0 B_{01} \int_{\nu} \psi(\nu) \phi_j(\nu) d\nu dV \quad (2.13)$$

In Equation 2.13, the absorption integral from Equation 2.11 is highlighted in red. The outer integral is performed in space, over the portion of the flame illuminated by the laser sheet. Under the assumption that the laser intensity is uniformly distributed over the sheet thickness, it is possible to rewrite the outer integral as a 1-D integral over the thickness of the flame by replacing the laser intensity, I with the laser power, P .

$$\Phi = \frac{P}{c} \int_x \frac{nA_{10}}{A_{10} + Q_{10}} f_0 B_{01} \int_{\nu} \psi(\nu) \phi_j(\nu) d\nu dx \quad (2.14)$$

Equation 2.14 is thus, the solution to the two-level model in the weak excitation limit. Note that the LIF signal varies linearly as the incident laser power (or intensity). Consequently, the weak excitation limit is also referred to as the linear regime.

For the sake of completion, we will briefly mention the other limit of the two-level model solution that occurs when the rate of pumping far exceeds the relaxation rate ($W_{01} \gg A_{10} + Q_{10}$). This is called the saturated limit and in this limit, the fluorescence signal ceases to change with the intensity of the incident laser beam. Operating in this regime is generally not preferred due to several reasons. First, the magnitude of the LIF signal per unit incident laser intensity tends to be the maximum in the linear regime. Once the variation ceases to be linear (even before nearing the saturation limit), we get diminishing returns for increasing the laser power. Further, the saturation criterion (maintaining a high laser intensity) is difficult to satisfy simultaneously in the spatial, temporal and spectral domains. For these

reasons, we will restrict our discussion hence forward the linear regime only.

2.2.2 CH PLIF Process

In this section, we will examine the limitations of trying to apply the two-level model to describe the CH PLIF process.

Laser-Induced Fluorescence is a multi-step process. First, the marker species absorbs a photon and transitions from a lower energy state to a higher one. This is followed by several physical processes, of which only one pathway leads to the spontaneous de-excitation of the excited molecule, accompanied by the release of a photon. The de-excitation can—but does not need to—take the molecule back to the original state. If the molecule does return to its original state, the fluorescence is said to be resonant. Due to the difficulty of measuring fluorescence signals at the same wavelength as the excitation beam, most practical applications of LIF tend to be non-resonant. The choice of the spectral and temporal properties of the excitation laser source, and of the detected fluorescence emission, constitute the excitation and detection schemes.

The excitation scheme chosen for this study follows the work done by Li et al.[\[13\]](#) who used a ring-cavity, pulsed alexandrite laser to provide excitation in the vicinity of the R-bandhead of the CH $B^2\Sigma^- \leftarrow X^2\Pi$ (0,0) system. This bandhead, shown in Figure [2.6](#), is found at a wavelength of about 387.2 nm and represents transitions from a ground state rotational quantum number of $N'' = 7$. When operated in multimode, alexandrite lasers have relatively large bandwidths (a few cm^{-1} is not uncommon) and hence make it possible to excite several of the neighboring transitions near the bandhead. The current implementation excites CH molecules in the ground state $X^2\Pi$, $v'' = 0$ with rotational quantum numbers N'' between 5–9.

Upon excitation, these molecules transition to the second electronically excited $B^2\Sigma^-$ state and populate the lowest vibrational level, ($v' = 0$). Since these transitions

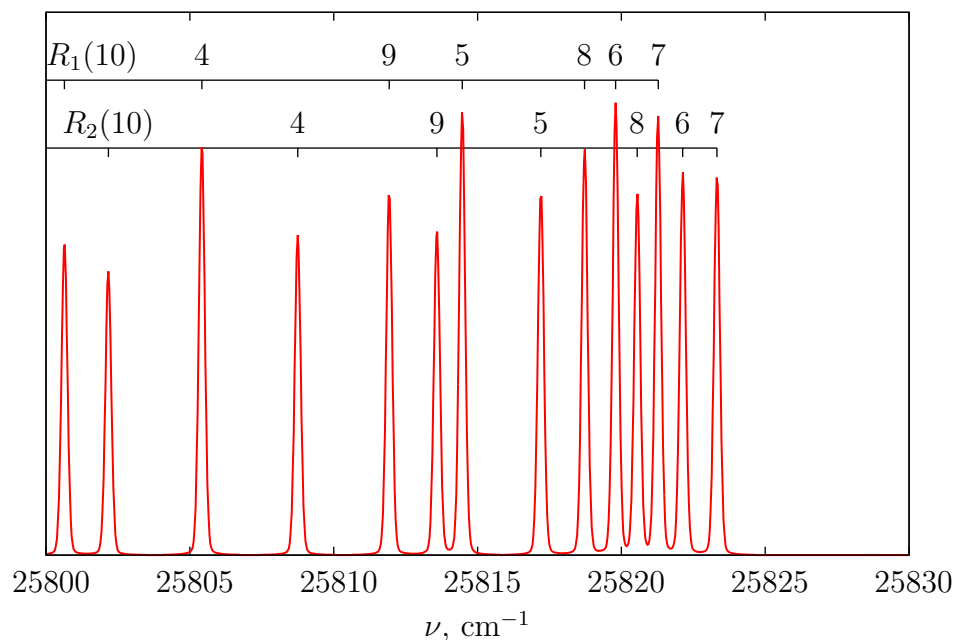


Figure 2.6: The figure shows the frequencies of the absorption lines near the R-bandhead of the CH $B^2\Sigma^- \leftarrow X^2\Pi$ (0,0) band. The individual lines are labeled with corresponding N'' quantum number.

occur in the R-branch, the rotational quantum number increases by +1, resulting in
the population of the N' levels between 6–10. At this point, the following possibilities
exist for the excited molecule:

1. The molecule can undergo inelastic collisions with other molecules, resulting in
relaxation in the rotational, vibrational or electronic manifolds.
2. The molecule can spontaneously emit a photon and return to any of the lower
energy states.
3. The molecule can experience stimulated emission in the presence of another
photon of the appropriate frequency and return to any of the lower energy
states.
4. The molecule can experience further excitation either by absorbing a photon or
through collisional means and can react chemically.

Now, let us examine these potential pathways in greater detail. The first pathway 591
pertains to relaxation. The excitation and subsequent population of a higher energy 592
state causes the CH population distribution to deviate from the equilibrium Boltz- 593
mann distribution. The degree of relaxation possible is limited by the lifetime of the 594
energy level the excited species occupy. The collision-free, radiative lifetime of the B 595
electronic state is about 300 ns[66]—long enough for sufficient rotational relaxation 596
to occur, but too short for complete vibrational relaxation. Based on experiments 597
conducted by Garland et al.[67], it is estimated that the vibrational energy transfer 598
between the two bound states available to the $B^2\Sigma^-$ state is about two orders of 599
magnitude slower than the rotational energy transfer. As a result, we may suppose 600
that the vibrational manifold remains relatively unaffected, while the rotational man- 601
ifold is relaxed closer to an equilibrium distribution. The question of the electronic 602
relaxation will be addressed later in this discussion. 603

The second option available for the excited CH molecule is to spontaneously emit a 604
photon and return to a lower energy state. Spontaneous de-excitation to the ground 605
state primarily follows the diagonal $B^2\Sigma^- \rightarrow X^2\Pi$ (0,0) band. The rate of such 606
spontaneous emission between two states is given by the Einstein emission coefficient 607
for the transition. Once again, we will defer discussion of the $B - A$ transition until 608
later in this discussion. 609

The third option is for the CH molecule to experience stimulated emission in 610
the presence of a photon of an appropriate frequency. It is highly unlikely that the 611
apposite photon would have a frequency other than the excitation laser. The rate 612
of stimulated emission induced by the excitation laser beam is proportional to the 613
Einstein absorption coefficient for the transition. Other photons that can induce 614
stimulated emission in the CH molecules could originate from spontaneous emission 615
or CH* chemiluminescence. As mentioned earlier, it is highly unlikely that these will 616
result in stimulated emission of any significant proportion. In part, this is due to 617

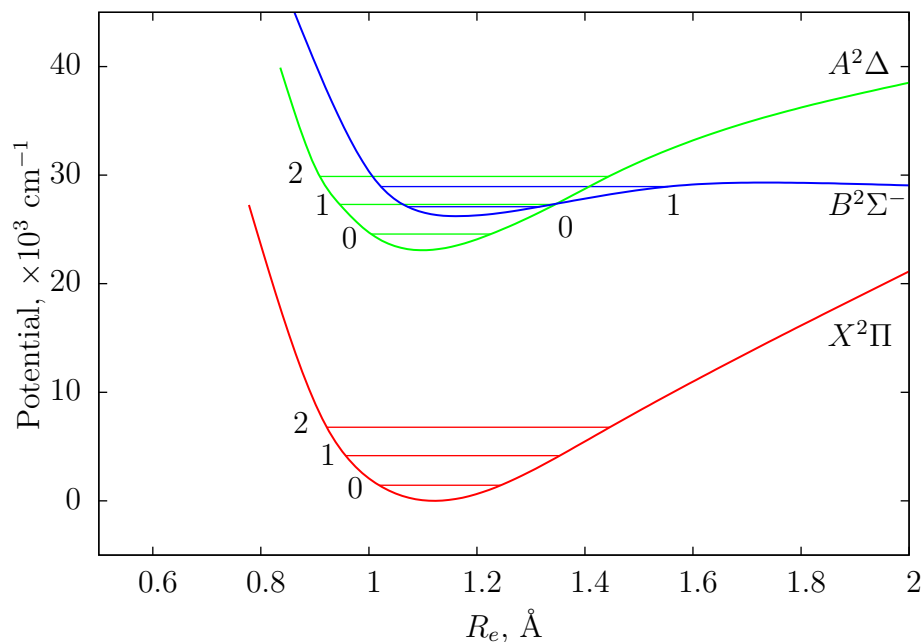


Figure 2.7: The figure shows the RKR potential curves for the $X^2\Pi$, $A^2\Delta$ and $B^2\Sigma^-$ energy levels in the CH system. A few vibrational levels are indicated for the $X^2\Pi$ and $A^2\Delta$ states. The $B^2\Sigma^-$ state has only two bound vibrational levels. The diagram is reproduced from Richmond et al.[68] who based it on ab initio calculations by van Dishoeck[69]

the spatial distribution of CH in a typical flame. In Chapter 1, it was stated that CH molecules are expected to be found only in the thin reaction zone of the flame. This causes most photons to be emitted in directions away from the flame, reducing their chance of encountering more CH molecules. Since CH is a minor species, its concentrations are inherently too low, further reducing the likelihood of this pathway.

The fourth option is for the molecule to experience further excitation by absorbing multiple photons or through collisions with other energetic molecules in the system. Since most available photons do not match any transitions from the $B^2\Sigma^-$, $v = 0$ state, it is unlikely to experience multi-photon excitation. However, collisional removal of CH molecules from the B state is certainly possible.

Having listed all the options, let us resume the discussion on the possibility of electronic energy transfer from the excited $B^2\Sigma^-$, $v' = 0$ state. The spacing of the energy levels in the CH system, shown in Figure 2.7, is such that the $B^2\Sigma^-$, $v' = 0$

state is found to be near-degenerate with the $A^2\Delta$, $v = 1$ energy level. Consequently, the $B^2\Sigma^- \leftrightarrow A^2\Delta$ (0,1) transition is reversible. Due to this, collisional population of the $A^2\Delta$ $v = 0, 1$ states from the $B^2\Sigma^-$ $v = 0$ state occurs rapidly. Garland et al.[67] measured that these transfers account for almost a quarter of all collisional depletion of the $B^2\Sigma^-$, $v = 0$ level. Theoretical calculations using overlap integrals between the involved energy levels predict that a majority of these transfers will be along the diagonal (0,0) transition.[70]. Instead, experimental data indicates that the number is closer to a fifth, with almost 80% of the transfers following the near-degenerate (0,1) pathway.

It is this electronic energy transfer mechanism that enables our excitation scheme to record high quality CH PLIF images. Having now populated the $A^2\Delta$ states, the resulting spontaneous emission from the $A^2\Delta \rightarrow X^2\Pi$ (0,0) and (1,1) transitions can be easily observed between 420–440 nm. A small portion of the fluorescence in this wavelength range also occurs from the $B^2\Sigma^- \rightarrow X^2\Pi$, (0,1) transition. Since these emission wavelengths are located far from the excitation wavelength, a simple glass filter is sufficient to suppress any elastic scattering from the laser beam.

2.2.3 Improved Model

While the two-level model is conceptually simple, applying it to describe the complicated physical process of CH PLIF is challenging. Daily[65] notes, for example, that significant errors can result from using the two-level model to describe even a three-level system. Hence, it is worthwhile to investigate a more complicated model that can describe the CH system with higher fidelity.

Figure 2.8 shows the relevant pathways that lead to the fluorescence emission as discussed in Section 2.2.2. An accurate model of the CH system should involve at least five energy levels, namely the $B^2\Sigma^-$, $v = 0$, $A^2\Delta$, $v = 0, 1$, and $X^2\Pi$, $v = 0, 1$ levels. The model will need to account for collisional transfers between each of these levels,



Figure 2.8: Some of the important transitions between energy levels in a CH molecule are shown. The excitation of the CH molecules (blue) is followed by collisional energy transfer processes (red) which populate additional energy levels. Spontaneous emission from some of these energy levels (green) is collected.

in addition to spontaneous and stimulated transitions. The mathematical solution 657
quickly becomes tedious and complicated. Further, it involves several rate coefficients 658
that have not yet been measured experimentally. 659

Fortunately, this can be significantly simplified. Previous studies[66, 70] have 660
indicated that the off-diagonal $B \rightarrow X$ (0,1) transition plays a relatively minor role 661
accounting for only 3.5% of the total fluorescence. Further, the radiative $A \rightarrow X$ 662
transitions are known[71] to be strongly diagonal, with little or no interaction[67] 663
between the two states. The net result of these two assertions is that we can treat 664
the two $B \rightarrow A \rightarrow X$ pathways to be disjoint and parallel. The resulting pseudo- 665
three-level model is shown in Figure 2.9. 666

According to this model, the lower state of the CH system is treated as a single 667
pool that CH molecules are excited from and returned to. This not only neglects 668
the rotational manifold, but also the vibrational manifold of the ground state. This 669
assumption would be valid as long as most of the CH molecules occupy the $v = 0$ 670
state and the fraction of molecules in the $v = 1$ state can be safely neglected. At 671
flame temperatures of about 2200 K, this assumption is somewhat questionable as 672
only about 83% of the ground state CH molecules occupy the $v = 0$ level and as much 673

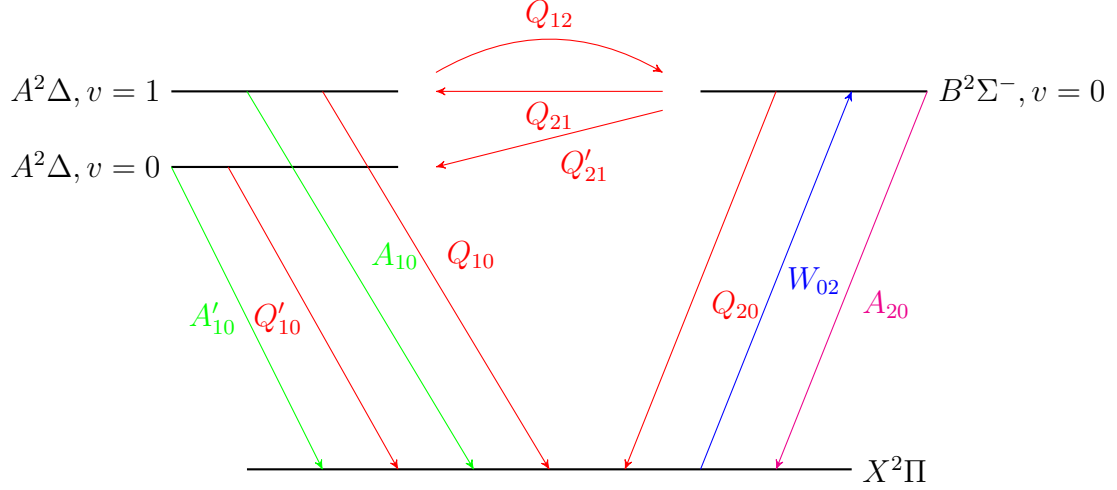


Figure 2.9: A simplified model of the transitions between the energy levels in a CH system. Excitation (blue) of ground state CH molecules to the upper electronic state is followed by several collisional energy transfer processes (red). A small portion of these molecules spontaneously emit a photon (green) and return to ground state. The spontaneous emission corresponding to resonant PLIF (magenta) is not collected.

as 14% are found at the $v = 1$ state. However, in light of the simplifications afforded
to our semi-quantitative model by this assumption, we retain it.

The rates of the various transition processes are indicated in Figure 2.9. W_{02} is
the pumping process that populates the $B(0)$ state. Q_{ij} are collisional energy transfer
processes that transfer CH molecules from the i level to the j level. The subscripts 0, 1
and 2 represent the electronic energy levels X , A and B . Processes involving the $A(0)$
state are differentiated from those involving the $A(1)$ state by a prime ($'$). Finally,
 A_{ij} represents the spontaneous emission coefficients between the i and j levels.

Applying Equation 2.6 to this case, we can write an expression for the LIF signal
intensity as follows,

$$\Phi = (n_1 A_{10} + n'_1 A'_{10})V \quad (2.15)$$

Our task is to solve for the values of n_1 and n'_1 in terms of n_0 . To do this we need
to write rate equations describing the variation of the populations of the three upper
states with time.

$$\frac{dn_1}{dt} = -(A_{10} + Q_{10} + Q_{12})n_1 + Q_{21}n_2 \quad (2.16)$$

$$\frac{dn'_1}{dt} = -(A'_{10} + Q'_{10})n'_1 + Q'_{21}n_2 \quad (2.17)$$

$$\frac{dn_2}{dt} = W_{02}n_0 + Q_{12}n_1 - (A_{20} + Q_{20} + Q_{21} + Q'_{21})n_2 \quad (2.18)$$

Under the assumption that the laser excitation time scale is much longer than the collisional time scales, we can set the LHS of Equations 2.16–2.18 to zero. This results in a closed set of linear equations, which can be expressed in matrix form as follows.

$$\begin{bmatrix} A_{10} + Q_{10} + Q_{12} & 0 & -Q_{21} \\ 0 & A'_{10} + Q'_{10} & -Q'_{21} \\ -Q_{12} & 0 & A_{20} + Q_{20} + Q_{21} + Q'_{21} \end{bmatrix} \begin{bmatrix} n_1 \\ n'_1 \\ n_2 \end{bmatrix} = \begin{bmatrix} 0 \\ 0 \\ W_{02}n_0 \end{bmatrix} \quad (2.19)$$

From Equation 2.19, we only need the solutions to n_1 and n'_1 . Substituting the solutions directly into Equation 2.15, we can write the solution in the following form to mirror the expression in Equation 2.8.

$$\Phi = n_0 V W_{02} (Y + Y') \quad (2.20)$$

The terms Y and Y' in Equation 2.20 are non-dimensional and represent the fluorescence yields from the two $A^2\Delta$ states. The functional expression for the yields is more complex now, as shown in Equations 2.21–2.22.

$$Y = \frac{Q_{21}A_{10}}{(A_{10} + Q_{10} + Q_{12})(A_{20} + Q_{20} + Q_{21} + Q'_{21}) - Q_{12}Q_{21}} \quad (2.21)$$

$$Y' = \frac{(A_{10} + Q_{10} + Q_{12})Q'_{21}A'_{10}}{(A'_{10} + Q'_{10})((A_{10} + Q_{10} + Q_{12})(A_{20} + Q_{20} + Q_{21} + Q'_{21}) - Q_{12}Q_{21})} \quad (2.22)$$

2.2.3.1 Absorption Integral Calculation

We now focus on the first portion of Equation 2.20 and consider the rate of population of the upper $B^2\Sigma^-$ state. As in case of the simple model, this term involves the computation of the integral of the product of the laser linewidth function, $\psi(\nu)$ and the absorption linewidth function, $\phi(\nu)$. However, since our excitation scheme targets multiple lines in the R-bandhead, we actually have a summation of several absorption lines in this integral.

$$\begin{aligned} W_{02} &= \frac{I}{c} \int \psi(\nu) \sum_j B_j \phi_j(\nu) d\nu \\ &= \frac{I}{c} \sum_j B_j \int \psi(\nu) \phi_j(\nu) d\nu \end{aligned} \quad (2.23)$$

In Equation 2.23, the terms B_j are the absorption coefficients, B_{02} , for each transition being excited, each of which has its own broadened linewidth, $\phi_j(\nu)$ at the local conditions. The discussion of the various sources of line broadening that need to be considered for our case is deferred till Chapter 4.

Equation 2.24 presents the expression for f_j in terms of the vibrational and rotational quantum numbers, (v, J) , of the energy level j .

$$f_j(v, J) = \frac{\exp\left(\frac{-hcE_v(v)}{kT}\right)(2J+1)\exp\left(\frac{-hcE_r(v, J)}{kT}\right)}{Q_{rv}} \quad (2.24)$$

The vibrational energy, $E_v(v)$ of a level is calculated according to Equation 2.25, while the rotational energy, $E_r(v, J)$ is calculated according to Equation 2.26.

$$E_v(v) = \omega_e \left(v + \frac{1}{2}\right) - \omega_e x_e \left(v + \frac{1}{2}\right)^2 + \omega_e y_e \left(v + \frac{1}{2}\right)^3 - \omega_e z_e \left(v + \frac{1}{2}\right)^4 \quad (2.25)$$

$$E_r(v, J) = \left\{B_e - \alpha_e \left(v + \frac{1}{2}\right)\right\} J(J+1) - \left\{D_e + \beta_e \left(v + \frac{1}{2}\right)\right\} J^2(J+1)^2 \quad (2.26)$$

The $B^2\Sigma^- \leftarrow X^2\Pi$ transition of the CH system is governed by Hund's Case b and hence, the appropriate rotational quantum number to use is N . For each rotational quantum number N , there are two possible values of J given by $N \pm \frac{1}{2}$. The rovibrational partition function, Q_{rv} is a summation over all available vibrational and rotational levels in the $X^2\Pi$ state. In practice, this summation over the vibrational states may be truncated at $v = 4$ and the summation over the rotational states may be truncated at $N'' = 22$ with negligible loss in accuracy. The values of the various spectroscopic constants in the above equations will be presented in Chapter 4.

2.2.3.3 Solution

721

The solution for the rate of production of fluorescence photons can be written in the following form that mirrors Equation 2.14.

722

723

$$\Phi = \frac{P}{c} \int_x n_{CH}(Y + Y') \sum_j f_j B_j \int_\nu \psi(\nu) \phi_j(\nu) d\nu dx \quad (2.27)$$

The expressions for the fluorescence yields, Y and Y' , still have many variables that have not been tabulated conveniently in literature. As a result, further simplifications will need to be made on the basis of reported experimental observations. These simplifications are outside the scope of this chapter and will be introduced in Chapter 4 along with the results of applying this model to various reactant mixtures.

724

725

726

727

728

CHAPTER 3

729

EXPERIMENTAL METHODS AND CONSIDERATIONS

730

The current chapter describes the experimental apparatus and the diagnostic approaches used in this work. The first section presents a detailed description of the LSB configurations that were tested, along with the testing facilities used for the experimental work. The second section focuses on the selection and implementation of the diagnostic techniques that were used to study flames and flow fields. Data reduction techniques used to process the acquired raw data are also described.

3.1 LSB Configurations

737

Two configurations of the Low Swirl Burner were tested for this study. These are referred to in what follows as Configurations A and B. Each configuration consists of the reactant flow inlet, the swirler device, the conduit to the combustion zone and the combustion zone itself. Figure 2.1 shows the design of the swirlers used for this study. Each swirler has an outer diameter, d_s , of 38 mm (1.5 in) and divides the flow into a central and annular portion. One of these configurations used swirlers with a perforated plate that had a concentric hole pattern as shown in the figure. The perforated plate induces a blockage in the central channel and controls the relative mass flow split between the two portions of the swirler. The key dimensions of the swirlers tested are presented in Table 3.1.

Each configuration is housed in a high pressure testing facility. The testing facility consists of an air and fuel supply system, a pressure vessel with adequate optical access and an exhaust system for the products. Each testing facility is instrumented to measure temperatures and pressures which are then used to calculate various flow

Table 3.1: *The dimensions of the swirlers used and the respective perforated plates are presented. Each swirler is referred to by its vane angle (as in “ S_{37° ”).*

Geometric parameter	Swirlers		
	Configuration A S_{37°	S_{45°	Configuration B S_{40°
Swirler data			
Outer diameter, d_s , mm	38	38	38
Diameter ratio, $\frac{d_i}{d_s}$	0.66	0.66	0.66
Vane angle, α	37°	45°	40°
Theoretical Swirl Number, S	0.48	0.64	variable
Perforated plate data			N/A
Open area, mm^2	155.97	156.98	-
Blockage, %	71.54	71.36	-
Plate thickness, mm	1.27	1.27	-
Hole pattern	1 - 8 - 16	1 - 8 - 16	-
Hole location (dia), mm	0 - 10.2 - 19.1	0 - 10.2 - 19.1	-
Hole diameter, mm	2.79 - 2.79 - 2.84	2.82 - 2.82 - 2.83	-

parameters of interest.

The design of the configurations tested, along with that of their respective test facilities are discussed in greater detail in this section.

3.1.1 Configuration A

Preliminary experiments involving velocity field mapping and flame imaging were performed using this configuration. The schematic of the high pressure test facility housing this configuration is shown in Figure 3.1, while the configuration itself is shown in greater detail in Figure 3.2.

3.1.1.1 Test Facility

Pressurized air is supplied from external tanks and heated in an indirect, gas-fired heat exchanger to about 500 K. The flowrate of the air is metered using a sub-critical orifice flow meter with a 38 mm (1.5 in) bore diameter Flow-Lin orifice plate capable

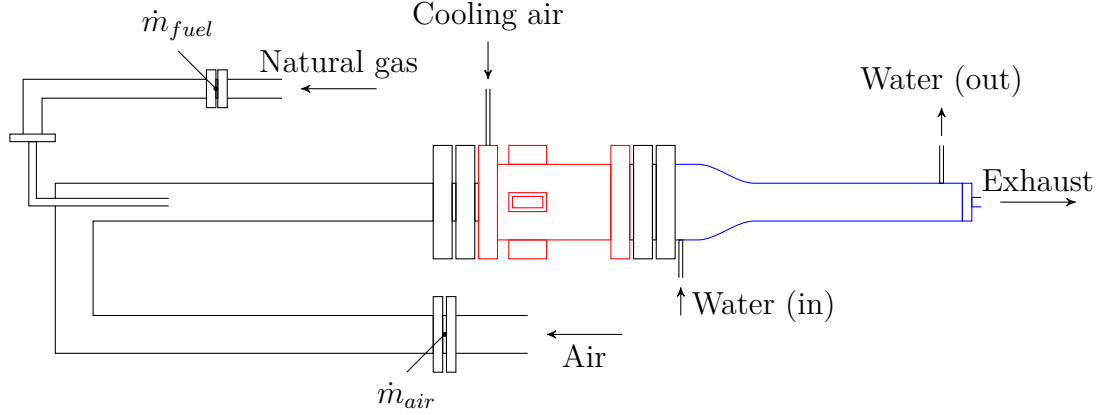


Figure 3.1: A schematic of the high pressure testing facility where Configuration A was operated is shown. The pressure vessel is outlined in red, while the water-cooled exhaust section is outlined in blue. The locations of the orifice flow meters used to measure the mass flow rates of the preheated air and natural gas fuel are indicated.

of metering a maximum flow rate of 2.2 kg/s (1 lb/s). The orifice flow meter is instru- 764
 mented with an Omega PX725A-1KGI pressure transmitter calibrated to a reduced 765
 pressure range of 0–2.758 MPa (0–400 psi), a shielded K-type thermocouple and an 766
 Omega PX771A-025GI differential pressure transmitter, calibrated to a reduced dif- 767
 ferential pressure range of 0–68.948 kPa (0–10 psid). The fuel (natural gas) is metered 768
 using a similar set up as the air line, with a sub-critical orifice flow meter. The fuel 769
 orifice plate is a Flow-Lin orifice plate with a bore diameter of 13.46 mm (0.53 in), 770
 capable of metering a maximum flow rate of 0.22 kg/s (0.1 lb/s). The upstream pres- 771
 sure is measured using an Omega PX725A-1KGI pressure transmitter (same as the 772
 air line) and the differential pressure is measured using a PX771A-100WDC differ- 773
 ential pressure transmitter with a pressure range of 0–2.489 kPa (100 in H₂O). The 774
 temperature of the fuel is assumed to be the same as the nominal room temperature 775
 (300 K). 776

The air enters the inlet nozzle of the LSB through a 1.8 m (6 ft) long, 102 mm (4 777
 in) diameter straight pipe section. The fuel flow is choked prior to mixing with the 778
 flow at the head of the straight pipe section. The straight pipe section allows for the 779
 flow to be fully developed, and fully premixed before the reactants enter the burner. 780

The combustor pressure and temperature are measured at the head of the inlet nozzle. 781
The pressure is measured by an Omega PX181B-500G5V pressure transducer with a 782
pressure range of 0–3.45 MPa (0–500 psi), while the temperature is measured using 783
a K-type thermocouple. 784

The pressure and temperature measurements are used to calculate the four pri- 785
mary flow parameters (combustor pressure, preheat temperature, reference velocity 786
and equivalence ratio) for the LSB in real time. All measurements are monitored and 787
recorded during the course of the experiment by a LabView VI. 788

The pressure vessel enclosing the combustor is designed to withstand pressures of 789
up to 30 atm and is insulated from the combustor by a ceramic liner. Cooling for the 790
pressure vessel and the quartz tube is provided by a flow of cold air introduced at the 791
head of the pressure vessel. The cold air is drawn from the same external tanks as 792
the main air line, but bypasses the heating system. The cold air flow is not metered, 793
but its upstream pressure is coupled to the main air line so as to ensure a steady flow 794
of cold air into the pressure vessel at all operating conditions. Optical access to the 795
combustor is provided through four 25 mm (1 in) thick, 150 mm (6 in)×75 mm (3 in) 796
quartz windows located 90° apart azimuthally. The view ports allow the combustor 797
to be imaged from the dump plane to an axial distance of 150 mm (6 in) downstream. 798

The exhaust from the combustor is cooled by cold water circulated through a 799
water jacket enclosing each section of the exhaust pipe. The length of the exhaust 800
pipe sections is about 1.8 m (6 ft). The exhaust pipe section terminates in an orifice 801
plug that provides back pressure to the combustion chamber. A different diameter 802
orifice is used for each reference velocity condition tested. The exiting products finally 803
pass through the building exhaust system. 804

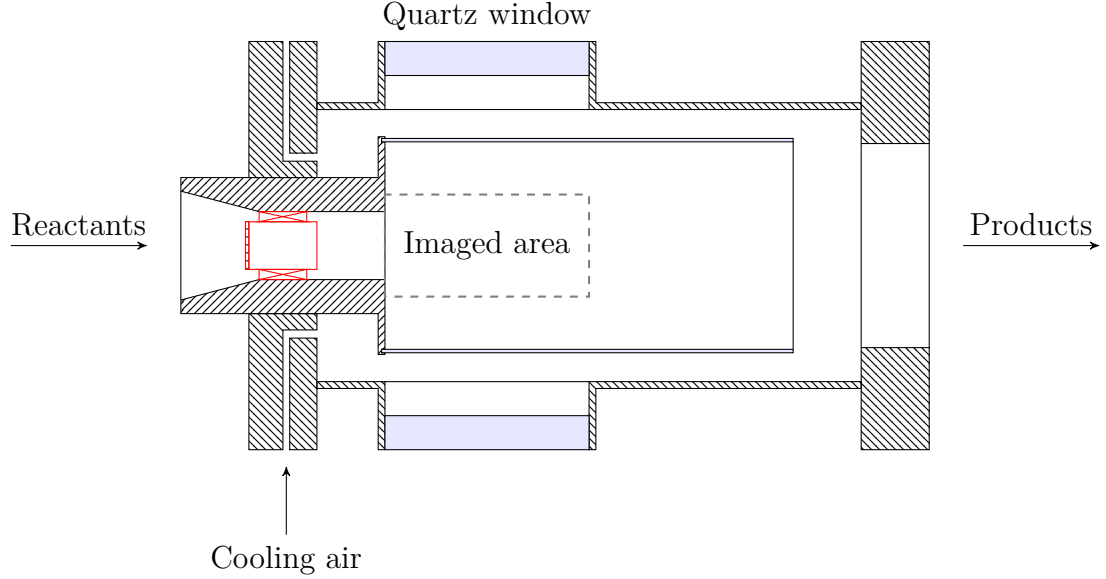


Figure 3.2: A cross-sectional view of Configuration A in the pressure vessel is shown. The reactants enter from the left. The products mix with the cooling air and leave on the right. The location of the swirler in the inlet nozzle is highlighted in red. Also shown is the region of the combustion zone that can be imaged through the quartz windows.

3.1.1.2 Low Swirl Burner

The detail of the LSB configuration is shown in Figure 3.2. The premixed, preheated reactants reach the swirler through a converging nozzle that decreases linearly in diameter from from the inlet diameter of 102 mm (4 in) to the outer diameter of the swirler, 38 mm (1.5 in). At the swirler, the flow splits into two streams—one passing through the central section and another picking up swirl by flowing over the vanes in the annular region. The relative flow split between the two streams is controlled by inducing blockage into the central flow by means of a perforated plate. The swirler leads to a constant area nozzle, and is located one diameter upstream of an abrupt area change. At the area change, the reactants expand from the 38 mm (1.5 in) diameter nozzle into a 115 mm (4.5 in) diameter combustion zone. This expansion ratio is chosen so as to avoid confinement effects on the centerline flame flow field.[28]

The main combustion zone begins at the dump plane and is enclosed by a GE 214 quartz tube. The quartz tube is 300 mm (12 in) long and 115 mm (4.5 in) in

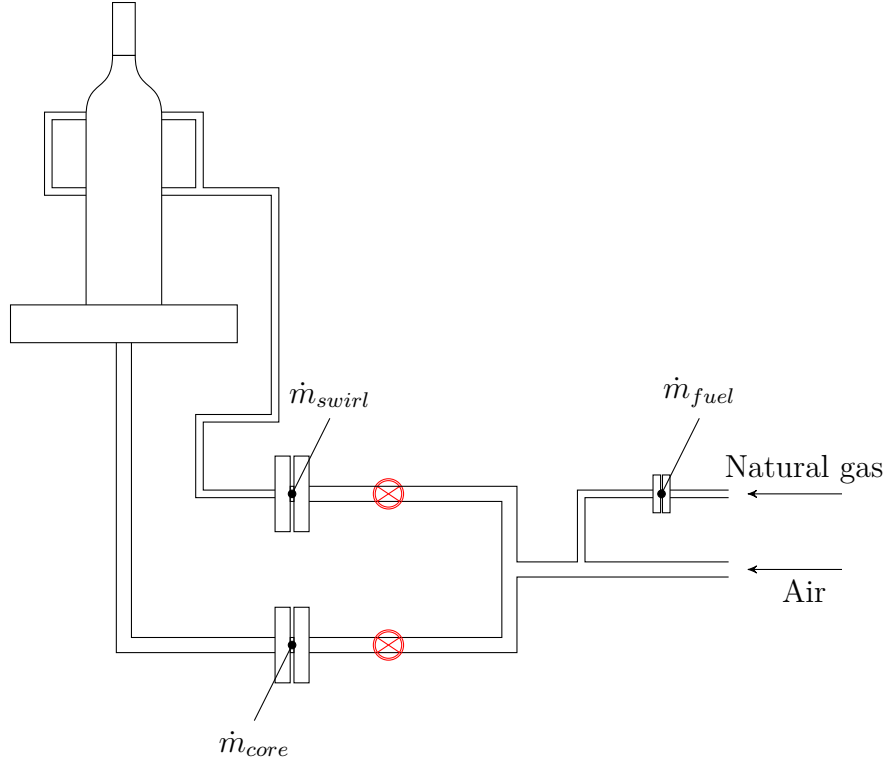


Figure 3.3: A schematic of the high pressure testing facility where Configuration B was operated is shown. The locations of the orifice flow meters on the reactant streams and fuel lines are shown. Valves (shown in red) on the swirl and core flow lines allow for the relative mass flow split to be varied between the two reactant streams. The upstream orifice flow meter on the preheated air line is not shown here. All preheated air lines are insulated.

diameter. The thickness of the quartz tube is 2.5 mm (0.1 in).

3.1.2 Configuration B

This configuration is used to image the flame structure of the LSB flame using CH PLIF. A schematic of the flow system of the test facility is shown in Figure 3.3, while the LSB combustor itself is shown in greater detail in Figure 3.4.

3.1.2.1 Test Facility

This test facility shares the upstream supply of preheated air and natural gas with the one used in Configuration A. The flow rate of the preheated air stream is measured using the same orifice flow meter system used in Configuration A—albeit with a

smaller 12.921 mm (0.5087 in) diameter bore Flow-Lin orifice plate. The fuel system pressure is regulated from the building supply pressure to a lower required pressure by an adjustable TESCO regulator and metered using a critical orifice flow meter. The critical orifice on the fuel line has a bore diameter of 0.8128 mm (0.032 in). The pressure upstream of the critical orifice is measured using an Omegadyne PX409-1.5KGI pressure transmitter with a range of 0–10.34 MPa (0–1500 psig) and the pressure downstream of the critical orifice is measured using a Dwyer 626 series pressure transmitter with a range of 0–3.45 MPa (0–500 psig). The downstream pressure can be used to verify if the critical orifice is choked during operation. The temperature of the fuel is measured upstream by a K-type thermocouple.

The air system is choked with a 5.41 mm (0.213 in) diameter critical orifice before mixing with the fuel. A short distance after mixing, the reactants are split into two separate streams for the central flow and the swirl flow. The central flow rate is measured using a 9.271 mm (0.365 in) diameter sub-critical orifice, instrumented with a Dwyer 626 series pressure transmitter with a range of 0–4.14 MPa (0–600 psig) for measuring the upstream pressure, a K-type thermocouple for measuring the upstream temperature and an Omega PX771-300WCDI differential pressure transducer with a range of 0–74.65 kPa (0–300 in H₂O). The swirl flow rate is measured similarly, using a 11.68 mm (0.46 in) diameter sub-critical orifice, a Dwyer 626 series pressure transmitter with a range of 0–5.52 MPa (0–800 psig), a K-type thermocouple and another Omega PX771A-300WCDI with a differential pressure range of 0–74.65 kPa (0–300 in H₂O). The relative flow split between the two reactant streams is controlled by partially closing gate valves on the two lines. All measurements are monitored and recorded by a LabView VI.

The test rig is designed to be operated with a pressure vessel and is rated for pressures as high as 30 atm. Unfortunately, the rig could not be operated at high pressure for the experiments performed in this study. The original design of the rig,

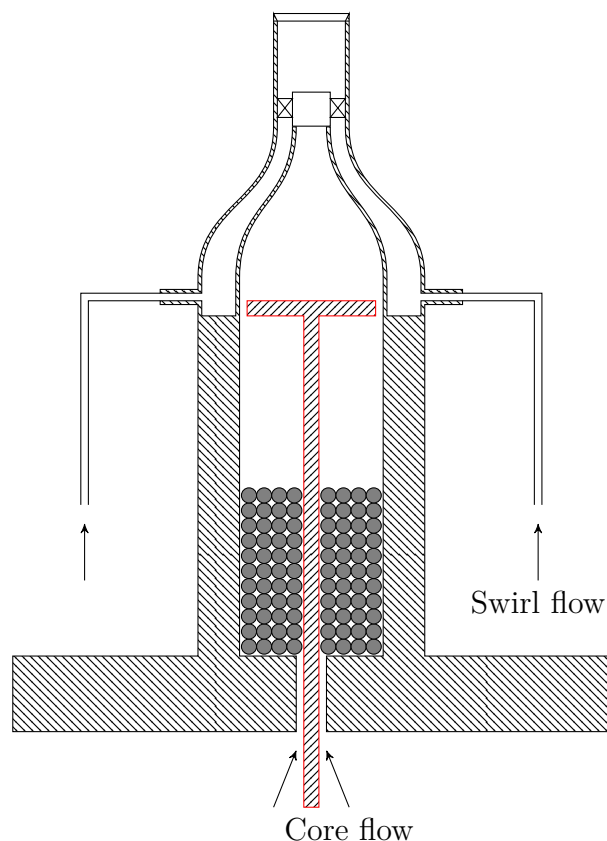


Figure 3.4: A cross-sectional view of Configuration B is shown. The core flow reactants enter through ports in the base flange. Stainless steel ball bearings partially fill the plenum chamber and render the core flow spatially uniform. The turbulence generator is located within the plenum and is outlined in red. The swirl flow reactants enter through separate pipes and are injected into the contoured nozzle through four ports.

developed for a separate program of research investigating turbulent flame speeds, 855
 was found to be incapable of successful operation at high pressure. As a result, the 856
 combustor was operated without a pressure vessel in the present work. The products 857
 are vented into the same building exhaust system as Configuration A. 858

3.1.2.2 Low Swirl Burner 859

The design of this LSB configuration is presented in Figure 3.4. As described ear- 860
 lier, the reactants reach the LSB swirler device through two separate streams. The 861
 core/central stream passes through a plenum chamber that is filled with steel ball 862
 bearings before approaching the swirler through a smoothly contoured nozzle with a 863

high contraction ratio. The annular/swirl stream reaches the swirler directly through
a separate contoured nozzle. The contraction ratio is chosen to inhibit the formation
of thick boundary layers in the reactant streams. The core stream passes through
the central portion of the swirler, while the annular stream picks up swirl by passing
through the vanes of the swirler. The swirler lacks a perforated plate covering the
central region as the primary function of the plate—regulating the relative mass flow
split—is performed by the test facility itself.

The swirler device is located at the beginning of a constant area nozzle which is
57.2 mm (2.25 in) in length. Following this, the reactants expand into the combustion
zone.

Unlike Configuration A, there is no dump plane or quartz tube to provide con-
finement to the combustion zone. The co-flow of cold air provides insulation to the
walls of the pressure vessel. Also, as mentioned earlier, the relative mass flow split
between the central and annular flows can be controlled directly. Finally, the level of
turbulence in the central flow can be adjusted by use of a turbulence generator[72]
located upstream in the plenum chamber.

3.2 Diagnostics

3.2.1 Laser Doppler Velocimetry

The velocity field of the LSB is mapped using a TSI 3-component LDV system.
Three wavelengths (514 nm, 488 nm and 476 nm) are separated from the output of a
5 W Argon ion laser by an FBL-3 multicolor beam generator. The individual beams
are split into two coherent beams, which are then focused to intersect and produce
interference fringes within an ellipsoidal measurement volume with dimensions of
the order of 100 μm . For this purpose, two transceiver probes are mounted 90° apart
about the axis of the LSB. The setup is illustrated in Figure 3.5. One transceiver probe

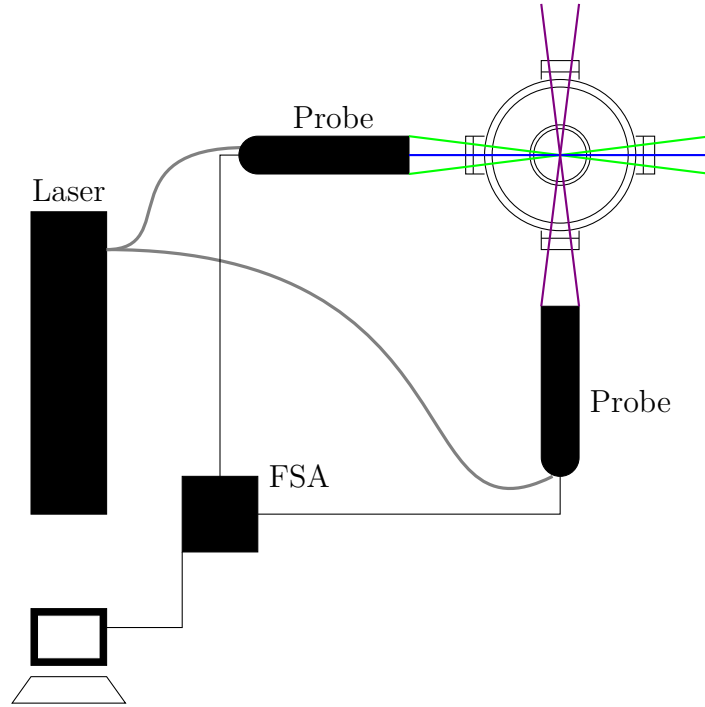


Figure 3.5: The schematic shows the setup employed to map the velocity field of the LSB combustor using Laser Doppler Velocimetry. Three pairs of orthogonal beams are separated from the Argon Ion Laser output and conveyed by fiber optic cables (gray) to optical probes mounted 90° apart about the axis of the LSB combustor. The green, blue, and violet beams in the schematic represent the 514 nm, 488 nm and 476 nm wavelengths. The signal is collected by the transceiver probes and analyzed by the FSA module. The results are saved for further analysis.

focuses the 514 nm and 488 nm beams in planes perpendicular to each other, while the
second probe focuses the 476 nm beams orthogonal to the other two beams. Particles
in the flow field crossing the interference fringes scatter the laser light elastically
and produce a sinusoidal signal whose frequency is proportional to the velocity of
the particle. The transceiver probes collect this scattered light and each wavelength
is detected separately by a PDM-1000-3 three-channel photodetector module. The
output from the photodetector is processed by an FSA-3500-3 signal processor. The
resulting three components of the particle/flow velocity are recorded by the FlowSizer
software.

Since the concentration of particulate matter (primarily dust particles) in the
airflow is very low, the flow needs to be artificially seeded to facilitate LDV measure-
ments in a reasonable amount of time. The choice of seeding particles to be used and
their mean diameter are decided by the characteristics of the flow to be imaged.[73]
Since the LSB flow field is a reacting one, the particles need to have high melting
points. Further, the particles need to be small enough to follow the flow closely and
large enough or reflective enough to scatter light efficiently in the measurement vol-
ume. Based on these requirements, commercially available alumina particles with a
mean particle diameter of 5 μm were chosen for this study. In order to uniformly seed
the flow, a novel seeding generator was designed as described in Appendix A. The
seeding particles were introduced slightly upstream of the 1.8 m (6 ft) long straight
pipe section in Test Rig A.

LDV data is only acquired at atmospheric pressure conditions. At high pressure
conditions, the reacting LSB flow field produces sharp refractive index gradients that
rapidly shift in the turbulent flow field. This causes strong beam steering effects
making it very difficult for the laser beams to reliably intersect within such a small
measurement volume.[74] The long distance traveled by the beams in the test rig
further exacerbate this problem, making LDV data nearly impossible to acquire at

such conditions.

916

3.2.2 CH* Chemiluminescence

917

The LSB flame is imaged using one of two 16-bit intensified CCD cameras—PI Ac- 918
ton 1024×256 or 512×512 pixels—with a 28 mm f/2.8 camera lens. The quantum 919
efficiency of the 18 mm Gen III HB filmless intensifier used by the 512×512 camera 920
is about 45% at 430 nm, while the 25 mm Gen II intensifier used by the 1024×256 921
camera manages about half that at the same wavelength. CH* chemiluminescence is 922
filtered using a bandpass filter centered on 430 nm with a FWHM of 10 nm. At each 923
operating condition, 100 instantaneous images are acquired with an exposure of 1 ms. 924
An additional 100 instantaneous images are acquired with no flame and averaged to 925
yield the background for correcting the flame images. 926

3.2.2.1 Image Processing

927

The acquired flame chemiluminescence images are background-corrected and aver- 928
aged. The resulting mean is the line-of-sight integrated, time-averaged image of the 929
flame. Strictly speaking, this is not the same as a real average obtained from a long 930
exposure image as the instantaneous images are obtained through a periodic sam- 931
pling process and hence, are prone to statistical errors. However, the behaviour of 932
the flame can be assumed to be sufficiently random that the mean obtained is ad- 933
equately representative of the true average. Figure 3.6a shows a typical mean CH* 934
chemiluminescence image prepared in this manner. 935

Even when background-corrected, the walls of the combustor are not at zero in- 936
tensity in the average chemiluminescence image. This is particularly noticeable near 937
the dump plane where there is no flame present and yet the walls are clearly illumi- 938
nated. The source of this background illumination is mostly the chemiluminescence 939
from the flame scattering off the combustor and pressure vessel walls. The contribu- 940



(a) *Average CH^* chemiluminescence image*



(b) *Centerline CH^* chemiluminescence intensity*



(c) *Abel deconvoluted half-image*

Figure 3.6: *These images illustrate the processing of a typical CH^* chemiluminescence dataset. The top image is the mean of 100 frames and shows the LSB flame at 9 atm. The flame standoff distance is calculated by locating the inflection point in the smoothed intensity profile (middle). An Abel deconvolution (bottom) can be used to highlight the flame brush and measure the angle of the flame.*

tion from blackbody radiation from the heated walls is less significant in the narrow 941
wavelength range imaged. This is evident from images acquired immediately after a 942
flame blowout, which show the walls to be nearly dark even though they should still 943
be hot. 944

The averaged chemiluminescence image allows us to measure the flame stand- 945
off distance by following the intensity profile along the centerline of the combustor. 946
The intensity profile rises sharply when passing the flame standoff location. Thus, 947
the flame standoff location can be ascertained by finding the inflection point in the 948
intensity profile. 949

The profile of the average chemiluminescence intensity along the centerline of the 950
sample case from Figure 3.6a is shown in Figure 3.6b, showing the flame standoff 951
distance. The distance from the dump plane, measured in number of pixels on the 952
image and scaled by the appropriate magnification factor yields the flame standoff 953
distance, X_f . The determination of the flame standoff location by this method pro- 954
vides a suitable and deterministic means to locating the leading edge of the flame 955
front. 956

The average image can be processed further to yield more spatially resolved in- 957
formation about the flame brush. Under the reasonable assumption that the average 958
LSB flame is axially symmetric about the centerline of the combustor, a tomographic 959
deconvolution technique called an Abel deconvolution[75] can be used to convert the 960
line-of-sight integrated image to a radial map of chemiluminescence intensity. In 961
effect, this shows the shape and structure of the average flame brush. The Abel 962
deconvolution of the sample data from Figure 3.6a is shown in Figure 3.6c. 963

The Abel-deconvoluted image provides a relatively easy means of determining the 964
flame brush angle. A straight line joining two points located at the center of the 965
flame brush intersects the axis of the combustor at this angle. The angle of the flame 966
is denoted by θ_f . 967



Figure 3.7: A schematic of the components of the PAL 101 Alexandrite laser is shown. The resonator formed by a High Reflection (HR) mirror and an output coupler is built around an alexandrite rod (red) pumped by flashlamps. The frequency of the output is selected by a tuner mechanism. Only one of the two Q-switches was used for this study. The laser beam is reduced in diameter by a collimating telescope (blue) before passing through the Second Harmonic Generator (SHG). The UV beam is separated from the fundamental by a dichroic mirror and exits the laser. The fundamental beam terminates within the laser in a beam dump.

Using the Abel deconvolution to study the flame brush suffers from two main drawbacks. First, the system of equations describing the Abel deconvolution is only valid as long as the entirety of the flame is visible. This is only satisfied in the initial region of the LSB where the diameter of the flame brush is smaller than the height of the optical viewport. At further downstream locations, the flame is not imaged in its entirety. This causes the spurious bright regions near the top of the window in Figure 3.6c. The second limitation of the Abel deconvolution technique stems from the high incidence of errors along the centerline (where $r \rightarrow 0$). Due to this, any study of the flame brush thickness at the flame stabilization point—a metric of considerable importance—is all but impossible using this tomographic technique.

3.2.3 CH Planar Laser-Induced Fluorescence

The CH PLIF setup uses the frequency-doubled output of a Light Age PAL 101 alexandrite laser tuned to $\lambda \approx 387.2$ nm. The design of the laser is shown schematically in Figure 3.7. The active medium is a 150 mm (6 in) long, 5 mm (0.197 in) diameter alexandrite rod. The rod is placed between two flashlamps within the resonator cavity formed by two spherical mirrors. A birefringent tuning element is

placed within the resonator to allow the user to select the frequency of the output 984
beam. The tuning element is coupled to a micrometer whose reading relates linearly 985
to the output wavelength. The birefringent filter allows the fundamental wavelength 986
to be varied between 720–780 nm, with peak gain at about 755 nm. The resonator 987
cavity also contains two Q-switches, which allow the laser to optionally operate in 988
double-pulsed mode. For this study, however, only one Q-switch is used and the laser 989
is operated in single-pulsed mode only. 990

The diameter of the fundamental beam exiting the output coupler is reduced by a 991
collimating telescope. This is done in order to increase the efficiency of conversion of 992
the frequency-doubling crystal. The second harmonic portion of the beam is separated 993
from the fundamental by a dichroic mirror and exits the laser. The fundamental beam 994
is terminated at a beam dump within the laser. The exit beam diameter is about 1 995
mm. 996

The alexandrite laser is capable of operating at frequencies of up to 15 Hz. Laser 997
power is controlled primarily by varying the voltage applied to the flash lamps. When 998
operating with a high flash lamp voltage, it is recommended that the frequency of 999
pulsing be reduced to allow more time to dissipate the heat build up within the 1000
alexandrite rod. All experiments conducted as part of this study operated the laser 1001
at 10.0 Hz. 1002

The typical power output of the laser is about 15 mJ/pulse. The pulsewidth of 1003
the laser is about 60-80 ns, as measured by a fast photodiode, and the pulsewidth 1004
decreases with increasing flash lamp voltage. The linewidth of the fundamental beam, 1005
as reported by the manufacturer, is 150 GHz at $\lambda = 775$ nm. Assuming the spectral 1006
profile of the laser to be a Gaussian, the linewidth of the frequency-doubled beam 1007
can be determined. The Full Width at Half Max (FWHM) of a Gaussian curve scales 1008
linearly with the standard deviation of the curve. When convoluted with itself, the 1009
new standard deviation is $\sqrt{\sigma^2 + \sigma^2}$ or $\sqrt{2}$ times that of the original curve. Thus, the 1010

linewidth of the frequency doubled output is $150 \times \sqrt{2} = 212$ GHz or 7.07 cm^{-1} . In 1011
wavelength units, this represents a spread of about 1.06 \AA . 1012

3.2.3.1 Imaging System 1013

All of the PLIF imaging is performed with an intensified PI Acton 512×512 camera. 1014
The intensified camera is equipped with an 18 mm Gen III HB filmless intensifier 1015
with a quantum efficiency of about 45% in the 420–440 nm range. The lens is chosen 1016
depending on imaging requirements of each experiment. In all imaging experiments, 1017
elastic scattering from the laser beam is attenuated by a 3 mm thick GG 420 Schott 1018
Glass filter. 1019

3.2.3.2 Laminar Flame Setup 1020

Preliminary experiments to evaluate the CH PLIF technique are performed on a 1021
laminar flame. The choice of a laminar flame as the subject allows us to neglect 1022
effects of strain and turbulence on the flame. Further, laminar flames are more readily 1023
simulated by reaction kinetics packages like Chemkin with high fidelity. 1024

These experiments are conducted on a laminar, methane-air flame stabilized on 1025
an unpiloted Bunsen burner with an inner diameter of 10.16 mm (0.4 in). The air 1026
flow rate is measured and regulated using a Dwyer rotameter with a range of 0–20 1027
SCFH calibrated using a Ritter drum-type gas meter. The natural gas flow rate is 1028
metered using a Matheson FM 1050 602 rotameter with a range from 0–1230 SCCM. 1029
This flowmeter is calibrated using a Sensidyne Gilibrator 2 bubble flow meter system. 1030

3.2.3.3 Laser Wavelength Calibration 1031

As described earlier, the output wavelength of the PAL 101 alexandrite laser is 1032
controlled using a micrometer-coupled birefringent tuning mechanism. The wave- 1033
length of the laser beam varies linearly with the micrometer reading. Initially, the 1034



Figure 3.8: The figure above shows the schematic of the experiment performed to calibrate the wavelength of the laser output. The laser output (containing mostly UV, but also a small portion of the fundamental frequency) is glanced off a steel optical post. The scattered light is gathered by a fiber optic cable (gray) and sent to a spectrometer. The spectrum is analyzed to track the location of the fundamental frequency with tuner position. The UV peak is not tracked as the spectrometer is not calibrated for that wavelength.

manufacturer-supplied calibration for the micrometer was found to be inaccurate. 1035
This required an experiment to calibrate the laser output wavelength against the mi- 1036
crometer reading in order to determine the slope and offset of the calibration curve 1037
accurately. 1038

A schematic of this experiment is shown in Figure 3.8. The laser beam is glanced 1039
off a steel optical post and the scattered light is collected using a fiber-optic cable cou- 1040
pled to an Ocean Optics HR 2000 spectrometer. The spectrometer is pre-calibrated 1041
using 50 wavelengths in the 400–850 nm range from the output of a neon discharge 1042
lamp source. The spectrometer is also intensity corrected over this range using a 1043
black body source. The estimated error in the resolution of the device is about 0.1 1044
nm (1 Å). 1045

The laser micrometer is traversed from 0.600 in to 0.625 in in steps of 0.001 in. 1046
The experiment is repeated by traversing the micrometer from 0.625 in back to 0.600 1047
in along the same points to ensure repeatability and estimate the variation due to 1048
hysteresis. The calibration is performed using at the fundamental wavelength of the 1049
laser as the second harmonic wavelength falls outside the spectrometer’s range. Each 1050

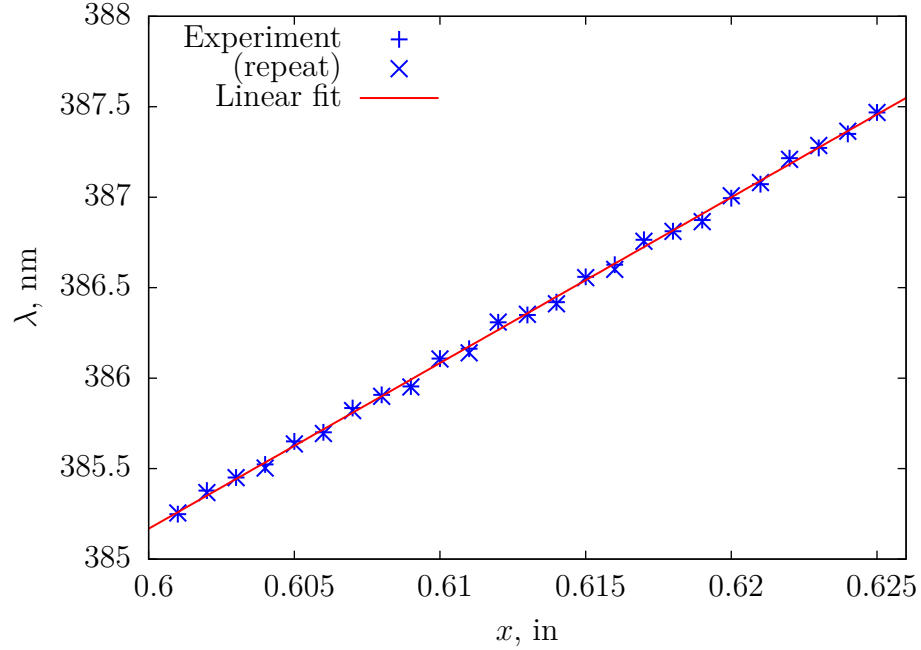


Figure 3.9: The wavelength of the second harmonic beam of the laser is plotted above against the tuner position(x). The data shows excellent repeatability and falls on a linear trend. The equation for the linear curve fit is $\lambda = 330.213 + 91.5908x$, where the units of λ and x are nm and in, respectively.

spectrum recorded is integrated over 512 ms and averaged over 10 such acquisitions. 1051
The background-corrected peak of the spectrum is then modeled as a Gaussian and 1052
the location of the center of the Gaussian waveform is recorded. 1053

The results from this experiment are shown in Figure 3.9. The plot demonstrates 1054
that the variation of the second harmonic wavelength (obtained by halving the fun- 1055
damental wavelength) with the position of the tuner micrometer is linear. Further, 1056
there is little difference between the measurements taken while increasing and de- 1057
creasing the micrometer position. This indicates that any effects of hysteresis in the 1058
micrometer position are minimal. The calibration equation relating the micrometer 1059
position to the output wavelength is obtained by applying a linear curve fit to the 1060
data points on the graph as shown in Figure 3.9. 1061

CHAPTER 4

1062

CH PLIF SIGNAL MODELING AND VALIDATION

1063

4.1 CH PLIF Preliminary Experiments

1064

The CH PLIF imaging system was evaluated for use in imaging hydrocarbon flames by performing two preliminary experiments. First, an excitation scan was performed to confirm the location of the optimal wavelength to excite the CH radicals in a typical hydrocarbon flame. Second, a test of the linearity of the LIF signal with respect to the incident laser intensity was performed. The setup and results of these experiments are described in the following subsections.

1070

4.1.1 Excitation Scan

1071

An excitation scan is performed by tuning the output of the alexandrite laser from $\lambda = 387.077$ nm to 387.260 nm. This serves two purposes. First, it locates the optimal wavelength to excite the CH radicals that results in the highest fluorescence yield. Second, the variation of the signal intensity can be compared with simulated profiles from LIFBASE or other spectroscopic calculations and our estimation of the laser linewidth can be validated. The laser linewidth is an integral parameter and appears in the absorption integral used by the models developed in Chapter 2.

1078

A schematic of the excitation scan experiment is shown in Figure 4.1. The intensified PI Acton 512×512 camera described in Section 3.2.2 is used to image a premixed, laminar methane-air flame operating at close to stoichiometric conditions. The laminar flame is stabilized on the Bunsen burner described in Section 3.2.3.2. The alexandrite laser is operated at a power of 16 mJ/pulse in the second harmonic. The sheet forming optics consist of a +50 mm cylindrical lens and a +250 mm spher-

1084

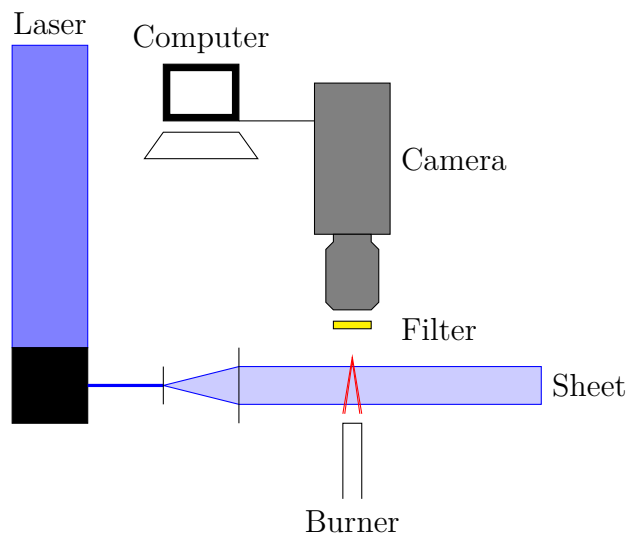


Figure 4.1: The figure above shows the schematic of the excitation scan experiment. A collimating pair of lenses form the laser beam into a sheet focused over a laminar Bunsen burner. The fluorescence is imaged perpendicularly by an intensified camera synchronized to the laser pulse. A 3 mm GG 420 filter is used to reject elastic scattering.

ical lens placed 300 mm apart. The optics form the beam into a collimated sheet 1085
about 25 mm (1 in) tall, focused to a thickness on the order of $250\ \mu\text{m}$ at the flame 1086
location. The sheet passes through the center of the flame and the edges of the sheet 1087
are blocked by razor blades to prevent reflections from the burner from saturating 1088
the camera. 1089

The induced fluorescence in the flame sheet is imaged perpendicularly by the in- 1090
tensified camera using an 85 mm f/1.8 Nikon AF Nikkor lens. A 3 mm thick 50 1091
mm \times 50 mm square GG 420 Schott glass filter is used to reject elastic scattering 1092
at the excitation wavelength. This setup gives a magnification of approximately 62 1093
 $\mu\text{m}/\text{pixel}$. The camera is triggered by the flash lamp sync signal from the laser sys- 1094
tem and the intensifier is gated over 300 ns, encompassing the 70 ns laser pulse. The 1095
long gate width gives the intensifier enough time to prepare to receive the fluores- 1096
cence, preventing signal loss due to irisng. The gate width is still short enough that 1097
minimal flame chemiluminescence or ambient lighting is recorded in the images. 100 1098
instantaneous images are acquired for each excitation wavelength to acquire a good 1099

estimate of the mean fluorescence signal, μ_{sig} .

Figure FIXME shows a sample CH PLIF image from this dataset. The images are background-corrected by subtracting the laser scattering (recorded without the flame). The fluorescence signal is calculated from these images using three alternate approaches.

In Method I, two “windows” are identified that include the straight sections of the laminar flame. The average fluorescence signal in each frame is calculated by taking the average of all the emitting pixels in the two windows. A pixel is designated as an emitting pixel if its intensity exceeds the standard deviation of a typical background pixel by at least a factor of five. The average of this value over all the frames is designated as the mean fluorescence signal, μ_{sig} . In Method II, the intensity of the pixels is integrated over a straight line connecting the inner and outer edges of the flame. The straight line is chosen along the beam so that the beam intensity does not vary along the integration path. The integration is performed on the left and right arms of the flame, giving two readings per frame. The mean of these values over all the frames is recorded as the mean fluorescence signal, μ_{sig} . In Method III, the midpoints of the straight lines from Method II are located and the average of their intensities, over all the frames is recorded as the mean fluorescence signal, μ_{sig} . The regions of interest for each of these methods is highlighted in Figure FIXME.

The result of this investigation is shown in Figure FIXME. The calculated mean fluorescence signals from the three methods are plotted against a LIFBASE simulation of the absorption spectrum of the CH $B-X$ transition. The profiles are appropriately scaled to match the LIFBASE simulation at the maximum value and at the minimum value. The LIFBASE simulation is performed for a thermalized system at 1800 K, at atmospheric pressure. Further, the instrument linewidth is specified to be the same as our estimate of the laser linewidth (1.06 Å).

The profiles of the calculated and scaled mean fluorescence signals are observed to

agree extremely well with the LIFBASE simulation result. The discrepancies between
the three methods is minimal.

The results indicate that the optimal excitation wavelength, corresponding to the
highest mean fluorescence signal, is about 387.2 nm. For the rest of the experiments
performed in this work, the laser is operated at this wavelength. The results also
help verify that the calibration of the micrometer is accurate and the wavelengths are
precisely adjustable. Finally, the results validate that our estimated laser linewidth,
1.06 Å, is accurate. This value can now be used in subsequent calculations of the LIF
signal levels.

4.1.2 Linearity Test

As explained in Chapter 2, the variation of the fluorescence signal with the excitation
laser intensity exhibits a saturation curve. For reasons mentioned in that discussion,
we prefer to operate in the weak excitation limit. Further, the models developed in
Chapter 2 for calculating the signal are intended to be used in the linear regime.
Hence, an experiment is performed to verify the linearity of the system response at
the intensities at which the flames are imaged for this work. The schematic of the
setup is shown in Figure FIXME. The laser is tuned to the optimal wavelength as
determined in Section 4.1.1, and operated at 10 Hz. The frequency-doubled beam is
directed at a steady, laminar, methane-air Bunsen flame operating at a slightly rich
stoichiometry. The edges of the beam are clipped by an aperture to produce a sharp
edge and to avoid unnecessary reflections from the burner. No optics are used to
refract the beam in any way.

The flame is imaged by the PI Acton 512×512 intensified camera equipped with a
50 mm, f/1.8 AF Nikkor lens. Elastic scattering is attenuated by a 3 mm thick GG 420
Schott glass filter. The magnification achieved by this set up is about 44 μm/pixel.
The LIF signal from the flame is recorded in 300 ns gates and accumulated 150 times

before being read out. For each case, a corresponding laser scattering image is also 1153
recorded for estimating the background. The flame chemiluminescence and ambient 1154
background are also recorded for the same purpose. 1155

For this experiment, varying the intensity of the laser beam by changing the flash 1156
lamp voltage or even the Q-switch timing is not preferred as either would alter the 1157
pulse width of the beam. Instead, quartz disks and blocks of varying thickness are 1158
introduced into the beam to produce an intensity loss, while preserving all other char- 1159
acteristics of the beam. The quartz elements decrease the intensity of the laser beam 1160
through reflection, scattering and absorption. The stray reflections and scattering 1161
from the quartz elements are contained by enclosing the elements in a box and pre- 1162
venting these from being recorded by the camera. In this manner, the laser power is 1163
varied from 10 mJ/pulse to 0.5 mJ/pulse and back. 1164

The acquired images are background-corrected and the intensity is conditionally 1165
averaged over pixels with a non-zero intensity in the region where the fluorescence 1166
occurs. The average fluorescence intensity values thus obtained are plotted against 1167
the corresponding laser intensity and shown in Figure FIXME. A sample image high- 1168
lighting the region of interest is also shown alongside. 1169

The LIF signal is observed to increase monotonically with increasing laser inten- 1170
sity. At the lower intensities, the variation is very nearly linear, with marginal scatter 1171
and only one significant outlier. At intensities above 1 J/cm² however, there is sig- 1172
nificant scatter in the data and the linear trend obtained from the low intensity cases 1173
cannot be reliably extended over this region. 1174

The results indicate that as long as the intensity of the laser sheet is kept below 1175
1 J/cm², the assumption of operating in the linear regime is valid. 1176

Table 4.1: *The coefficients of spontaneous emission for transitions in the CH system are provided.*

Transition	Symbol	A, s ⁻¹
$B \rightarrow X(0, 0)$	A_{20}	2.963×10^6
$A \rightarrow X(1, 1)$	A_{10}	1.676×10^6
$A \rightarrow X(0, 0)$	A'_{10}	1.832×10^6

4.2 Fluorescence Signal Modeling

Chapter 2 presented analysis of LIF signal calculation as a function of thermodynamic conditions and the local composition in a flame. Expressions derived using a basic model (Equation 2.14) and a more complex model (Equation 2.27) were presented. The expressions rely on knowledge of several physical values and specific spectroscopic constants pertaining to the CH system.

The basic model requires us to know the Einstein coefficient for spontaneous emission from the “upper” state to the “lower” state. For this, we assume that the “upper” state has the same properties as the $A^2\Delta$, $v = 0$ state. The improved model, needs the emission coefficients for the $B^2\Sigma^-$, $v = 0$ and $A^2\Delta$, $v = 0, 1$ states. These are tabulated from sources in literature[71, 76] FIXME in Table 4.1.

Next, to calculate the fluorescence yield for the basic model, we need to know the quenching cross-sections of major species found in the flames of interest. These cross sections are curve-fitted from several experiments performed over varying ranges of temperature. The functional forms of these cross-sections are presented in Table 4.2.

The fluorescence yield expressions for the complex model require the rates of collisional transfer between several energy levels. There have been efforts to measure and model these rates, but the energy level model used for these studies is more complicated and cannot be easily reconciled with our simplified model. Hence, it would be preferable to make some simplifying assumptions so that the collisional

Table 4.2: *The functional form of the quenching cross-sections of various species with CH are provided.*

Species	$\sigma, \text{\AA}^2$
H ₂	$6.1 \exp(-686/T)$
H	$221T^{-0.5} \exp(-686/T)$
O ₂	$8.61 \times 10^{-6} T^{1.64} \exp(867/T)$
OH	$221T^{-0.5} \exp(-686/T)$
H ₂ O	9.6
CH ₄	$52.8T^{-0.5} \exp(-84/T)$
CO	8.31
CO ₂	$8.67 \times 10^{-13} T^{3.8} \exp(854/T)$
C ₂ H ₆	13.4
N ₂	$1.53 \times 10^{-4} T^{1.23} \exp(-522.1/T)$
C ₃ H ₈	22

rates can be reduced in terms of the quenching rate.

Previous work has reported that the rate of quenching does not appreciably vary over the vibrational manifold, but excited CH molecules in the $B^2\Sigma^-$ electronic state are approximately 30% more likely to be quenched than molecules in the $A^2\Delta$ states. This allows us to eliminate Q'_{10} and Q_{20} as follows.

$$Q'_{10} = Q_{10} = Q \quad (4.1)$$

$$Q_{20} = 1.3Q \quad (4.2)$$

Our next assumption is based on work by Luque et al.[70] FIXME who reported that the rate of transfer following the $B^2\Sigma^- \rightarrow A^2\Delta (0,1)$ transition accounts for almost 24% of the collisional removal of CH from the upper electronic state. This allows us to formulate one more equation as shown below.

$$\frac{Q_{21} + Q'_{21} - Q_{12}}{Q_{20} + Q_{21} + Q'_{21} - Q_{12}} = 0.24 \quad (4.3)$$

$$\therefore \frac{R_{21} + R'_{21} - R_{12}}{Q} = 0.4105 \quad (4.4)$$

Next, using the reported results from the same authors[70] FIXME, we know that 1206
the number of CH molecules following the $B^2\Sigma^- \rightarrow A^2\Delta$ (0,1) transition is four times 1207
as much as the number following the $B^2\Sigma^- \rightarrow A^2\Delta$ (0,0) transition. 1208

$$\frac{Q_{21} - Q_{12}}{Q'_{21}} = 4 \quad (4.5)$$

Finally, Garland et al.[67] FIXME reported that the rate of the forward transfer 1209
along the $B^2\Sigma^- \rightarrow A^2\Delta$ (0,1) transition is about 60% faster than the reverse process. 1210

$$\frac{Q_{21}}{Q_{12}} = 1.6 \quad (4.6)$$

This gives us the third equation forming a closed, linear set of equations in terms 1211
of Q_{21} , Q_{12} and Q'_{21} that can be written out in matrix form and solved. Equation 4.7 1212
presents the solution. 1213

$$\begin{bmatrix} R_{21} \\ R'_{21} \\ R_{12} \end{bmatrix} = \begin{bmatrix} 5.1966 \\ 0.4872 \\ 3.2479 \end{bmatrix} Q \quad (4.7)$$

Substituting Equations 4.1, 4.2 and 4.7 into Equations 2.21–2.22 leads to sim- 1214
plified expressions for the two fluorescence yields. More importantly, they are now 1215
functionally dependent on only the Einstein coefficients and the rate of collisional 1216
quenching. 1217

Table 4.3: *FIXME*The coefficients of absorption for selected transitions in the CH X($v = 0$) system are provided.

N''	J_1''	ν_1 cm ⁻¹	$B \times 10^{-9}$ m ² J ⁻¹ s ⁻¹	J_2''	ν_2 cm ⁻¹	$B \times 10^{-9}$ m ² J ⁻¹ s ⁻¹
1	0.5	25756.08	6.511	1.5	25774.03	5.823
2	1.5	25776.42	7.225	2.5	25782.72	6.489
3	2.5	25792.74	7.532	3.5	25797.06	7.174
4	3.5	25805.42	7.671	4.5	25808.75	7.460
5	4.5	25814.47	7.719	5.5	25817.20	7.581
6	5.5	25819.80	7.708	6.5	25822.13	7.610
7	6.5	25821.28	7.652	7.5	25823.32	7.581
8	7.5	25818.72	7.561	8.5	25820.55	7.506
9	8.5	25811.93	7.439	9.5	25813.59	7.396
10	9.5	25800.64	7.288	10.5	25802.17	7.254
11	10.5	25784.57	7.111	11.5	25785.98	7.083
12	11.5	25763.38	6.907	12.5	25764.70	6.884
13	12.5	25736.65	6.676	13.5	25737.88	6.657
14	13.5	25703.90	6.418	14.5	25705.06	6.402
15	14.5	25664.54	6.129	15.5	25665.64	6.116
16	15.5	25617.87	5.815	16.5	25618.92	5.804
17	16.5	25563.03	5.472	17.5	25564.03	5.463
18	17.5	25499.00	5.101	18.5	25499.95	5.094
19	18.5	25424.52	4.624	19.5	25425.42	4.618
20	19.5	25338.08	4.161	20.5	25338.93	4.156
21	20.5	25237.84	3.674	21.5	25238.64	3.670
22	21.5	25121.60	3.183	22.5	25122.36	3.180

$$Y_1 = \frac{5.1966Q}{(A_{10} + 4.2479Q)(A_{20} + 6.9838Q) - 16.8780Q} \quad (4.8)$$

$$Y_1' = \frac{0.4872Q(A_{10} + 4.2479Q)}{(A_{10}' + Q)((A_{10} + 4.2479Q)(A_{20} + 6.9838Q) - 16.8780Q)} \quad (4.9)$$

The calculation of the quenching rate also requires us to know the number density ¹²¹⁸ of the major species in the flame zone. The profile of the local mole fractions of ¹²¹⁹ various species through a 1-D, freely propagating, laminar flame was obtained from ¹²²⁰ CHEMKIN solutions using the Flame-Speed Calculator reactor model. Results are ¹²²¹

presented in this chapter for laminar flames using a variety of reactant mixtures and inlet conditions. Additional results for strained laminar methane-air flames are calculated using the Opposed flow flame reactor model.

The CHEMKIN results provide mole fractions, which can be used to solve for the number density of each species using the following equation.

$$n_i = \frac{pN_A X_i}{RT} \quad (4.10)$$

In Equation 4.10, N_A is Avogadro's number, X_i is the mole fraction of species i , R is the universal gas constant and p , T are the local pressure and temperature in the flame.

Next, in order to calculate the absorption integral, we require the Einstein B-coefficients, along with the line positions of the transitions excited by the laser. These are taken from FIXME and tabulated in Table 4.3. Using these values, it is possible to calculate the optimal laser wavelength that results in the highest value of the absorption integral. The optimal laser wavelength is not a constant value and depends on the temperature and pressure at which the CH molecules are present. Using a typical value of 1800 K for the temperature in the flame zone, the variation of the optimal laser wavelength can be plotted against combustor pressure. As the combustor pressure increases, the absorption lines in the CH $B^2\Sigma^- \leftarrow X^2\Pi$ (0,0) R-bandhead are increasingly broadened by collisional broadening. Absorption lines that are at slightly lower frequencies, but close to the bandhead can now begin to absorb the laser energy. This causes the optimal laser wavelength to move slightly towards smaller wavenumbers. Figure FIXME shows this variation.

During experiments, this shift contributes negligibly towards increasing the LIF signal and hence, the laser tuner can be left at the optimal location for atmospheric pressure cases.

Returning back to Equations 2.14 and 2.27, we need spectroscopic constants of

Table 4.4: *Spectroscopic constants for the CH X²Π level are presented.*

Constant	Value, cm ⁻¹
ω_e	2860.7508
$\omega_e x_e$	64.4387
$\omega_e y_e$	0.36345
$\omega_e z_e$	-1.5378×10^{-2}
B_e	14.459883
α_e	0.536541
D_e	1.47436×10^{-3}
β_e	-2.530×10^{-5}

the X²Π, $v = 0$ energy level in order to calculate the Boltzmann fractions, f_j . These constants have been determined by Zachwieja et al.[77] and are tabulated in Table 4.4.

Next, FIXME, we discuss broadening mechanisms and the analytical expression for the absorption integral.

Consider now, each term in the above integral. The laser lineshape function, $\psi(\nu)$, can be modeled as a Gaussian profile without any loss of generality. The linewidth of the alexandrite laser, when operated in broadband mode, is of the order of a few wavenumbers. The effect of line broadening mechanisms, such as natural broadening, inhomogeneous broadening, etc that are commonly encountered in solid state lasers are negligible in comparison and hence, do not affect the lineshape appreciably.

$$\psi(\nu) = \frac{1}{\sigma_l \sqrt{2\pi}} \exp\left(-\frac{(\nu - \nu_l)^2}{2\sigma_l^2}\right) \quad (4.11)$$

The mean of the lineshape profile, ν_l , is set by tuning the center wavelength of the laser. The Full Width at Half Max (FWHM) of the laser, $\Delta\nu_l$, is prescribed by the manufacturer and can be used to calculate the standard deviation of the Gaussian as

follows.

1261

$$\sigma_l = \frac{\Delta\nu_l}{2\sqrt{2\ln 2}} \quad (4.12)$$

The lineshape of the absorption line being excited, on the other hand, is primarily dictated by mechanisms associated with gas-phase media—collisional broadening and Doppler broadening being the most important ones. Collisional broadening is a homogeneous mechanism and produces a Lorentzian broadened lineshape. The FWHM of the Lorentzian profile is related to the thermodynamic conditions by the following empirical formula.

1262
1263
1264
1265
1266
1267

$$\Delta\nu_c = 0.1 \left(\frac{p}{p_0} \right) \left(\frac{T_0}{T} \right)^{0.6} \quad (4.13)$$

In Equation 4.13, p_0 and T_0 represent standard conditions of pressure and temperature (101325 Pa and 300 K) respectively. By contrast, Doppler broadening is an inhomogeneous mechanism that results in a Gaussian lineshape. Its effect depends on the frequency (wavenumber) of the line being broadened, ν_a , and on the molecule's velocity. The FWHM of the resulting broadened lineshape is given by,

1268
1269
1270
1271
1272

$$\Delta\nu_d = \nu_a \frac{\sqrt{\ln 2}}{c} \sqrt{\frac{8kT}{m_{CH}}} \quad (4.14)$$

The combined effect of these two broadening mechanisms can be calculated by convoluting the two broadened lineshapes. **FIXME:** Note that this assumption is fine if the dominant broadening mechanism is Doppler broadening. However, in combustion systems, particularly at pressure, the dominant mechanism is collisional broadening, making the curve much closer to a Lorentzian shape. In this case, a Lorentzian convoluted with a Gaussian results in a Voigt profile. Lorentzian profiles have more area in the “wings” of the curve than Gaussian profiles. However, since the maximum broadening of the absorption lines is smaller than the linewidth of the laser beam,

1273
1274
1275
1276
1277
1278
1279
1280

this should not affect our results too much. FIXME: Perhaps a test using a Voigt profile vs a Gaussian profile to model absorption?

In order to simplify the calculations, we assume that the collision-broadened Lorentzian profile is reasonably approximated by a Gaussian profile with the same FWHM. Now, the convolution of the two profiles results in another Gaussian, with the same mean and a FWHM given by,

$$\Delta\nu_a = \sqrt{\Delta\nu_c^2 + \Delta\nu_d^2} \quad (4.15)$$

Thus, the Gaussian lineshape of the broadened absorption line can be written as,

$$\phi(\nu) = \frac{1}{\sigma_a \sqrt{2\pi}} \exp\left(-\frac{(\nu - \nu_a)^2}{2\sigma_a^2}\right) \quad (4.16)$$

In Equation 4.16, ν_a is the frequency (wavenumber) of the absorption peak being excited. The standard deviation of the lineshape, σ_a , is related to the broadened FWHM, $\Delta\nu_a$, by the following equation.

$$\sigma_a = \frac{\Delta\nu_a}{2\sqrt{2\ln 2}} \quad (4.17)$$

With the above information, the integral in Equation 2.23 can be solved analytically as follows.

$$\int \psi(\nu)\phi(\nu)d\nu = \frac{1}{\sqrt{2\pi(\sigma_a^2 + \sigma_l^2)}} \exp\left(-\frac{(\nu_l - \nu_a)^2}{2(\sigma_a^2 + \sigma_l^2)}\right) \quad (4.18)$$

This formulation of the signal intensity implicitly makes the following assumptions.

1. The fluorescence emission is predicted at steady state.
2. The collection volume is optically thin and an emitted photon is not reabsorbed within the flame itself. This is a reasonable assumption to make, since the flame thickness and the thickness of the laser sheet are both typically quite small.

4.3 Results

1298

Comparison of CH concentration predicted by GRI Mech and San Diego mechanisms 1299
for methane. 1300

CHAPTER 5

1301

LSB FLAME CHARACTERISTICS

1302

In Chapter 2, we introduced the salient features of the Low Swirl Burner (LSB) flow field and discussed the mechanisms by which the LSB flame is stabilized. Further, various characteristics of the LSB flame that can be measured from flame images were outlined. To recapitulate, these are the flame location, flame shape and the flame structure. The first two are quantified by the flame standoff distance, X_f , and the flame angle, θ_f , respectively.

1303
1304
1305
1306
1307
1308

In the same chapter, we introduced the four flow parameters that describe an operating condition for the LSB — the combustor pressure, p , the preheat temperature, T , the mass-averaged inlet velocity (also called the reference velocity, U_0), and the equivalence ratio of the premixed reactants, ϕ . We further introduced a geometric parameter — the angle of the vanes of the swirler, α , which affects the amount of swirl present in the flow field.

1309
1310
1311
1312
1313
1314

The LSB flame was studied over a range of operating conditions, and the effect of flow and geometric parameters on the reacting flow field were investigated. The results of these investigations are presented in this chapter.

1315
1316
1317

5.1 Effect of Reference Velocity

1318

In typical gas turbine applications, varying the loading on the engine does not affect the reference velocity. However, since the reference velocity is a design parameter, the effect it has on the flame characteristics has implications for the design of future LSB-based gas turbine engines.

1319
1320
1321
1322

One of the key objectives of this thesis is to investigate how the LSB flame stabi-

1323

lization operates at high pressure conditions. The simple model described in Chapter 2 predicts a self-similar flow field for the LSB at all reference velocities. This implies that the reference velocity will have no discernible impact on the flame standoff distance. This result is desirable for gas turbine designers, since the flame location and shape can be assumed to be constant. Limited testing conducted in published works confirmed this behavior at atmospheric pressure conditions with no preheat.

In order to verify the validity of this model at high pressure conditions in the presence of substantial preheat, the LSB was operated at a pressure of 6 atm over a range of reference velocities from 10 m/s to 40 m/s. For these tests, the S_{37° swirler was used. In a parallel series of tests, the S_{45° swirler was tested at a pressure of 3 atm at a reference velocities of 40 and 80 m/s. The location of the flame was measured from CH* chemiluminescence images, and the results are presented in Figure FIXME.

There is essentially no systematic variation in the flame standoff distance or the flame angle for the low velocity, S_{37° tests. Based on the model, this can be interpreted as the increase in reference velocity producing a concomitant increase in the turbulent flame speed at the flame stabilization location, negating any change in the flame's location. In other words, the flow field appears to retain its self-similarity, even at elevated pressures and temperatures.

When the S_{45° swirler was tested at higher reference velocities, however, the flame location shifted downstream sharply. This indicates potential limitations to the simple flame stabilization model that may not predict the behavior of the LSB flame at elevated pressures and temperatures, particularly at high reference velocities.

A possible cause of this limitation can be explored by considering the effect of increased reference velocity on the turbulent combustion regime in which the LSB combustor operates. Previous studies have primarily operated the LSB in the flamelet regime where the modified Damköhler model predicts the behavior of the turbulent flame speed with reasonable fidelity. At elevated pressures, both the laminar flame

speed of the reactants, S_L and the flame thickness, δ_f are diminished. This places
the operating regime higher and more to the right on a Borghi diagram, as shown in
Figure FIXME. While increasing the reference velocity did not affect the turbulent
combustion regime at lower pressures in a flamelet combustion regime, at elevated
pressures the flame may be transitioning into the thin reaction zone regime. This
transition would cause a reduction in S_T/S_L , or at least a lesser increase, and the
turbulent flame speed would no longer be expected to increase in step with U_0 and
the increased levels of turbulence. This would explain the the observed downstream
shift of the high pressure LSB flame at high reference velocities.

5.2 Effect of Preheat Temperature

The preheat temperature of the reactants is a key flow parameter, especially for gas
turbine combustors. In general, the rates of most chemical reactions in the flame zone
are highly sensitive to the temperature of the reactants. For the LSB in particular,
the temperature of the incoming flow directly affects its viscosity and consequently,
the velocity field in the flame stabilization region. Thus, studying the effect of the
preheat temperature on the LSB flame and flow field is important.

In order to explore this in greater detail, the velocity field of the combustor was
mapped using Laser Doppler Velocimetry (LDV). The conditions were chosen to study
the effect of increasing the preheat temperature on both reacting and non-reacting
LSB flow fields. Further, the study includes both low and high reference velocity cases.
The relevant flow parameters relating to these tests are presented in Table FIXME.
All LDV tests were limited to atmospheric pressure conditions. Implementing the
LDV technique at elevated pressures proved difficult due to beam steering issues,
coupled with impractical turn-around times between the successive runs that would
be required to obtain sufficient LDV data points for analysis.

The normalized centerline mean and rms axial velocity profiles for the three cases

are presented in Figure FIXME. The abscissa represents the distance from a point 1377
called the virtual origin, X_0 . The virtual origin is defined as the imaginary location 1378
where the extrapolated linear axial velocity profile reaches the reference velocity in 1379
magnitude. The extrapolation is indicated in Figure FIXME by a dashed line. 1380

As noted in Chapter 2, previous studies[34] reported that mean axial stretch 1381
— the normalized slope of the linear decay of axial velocity — at the inlet of the 1382
combustor was self-similar, regardless of the Reynolds number, Re of the operating 1383
condition. Further, it was reported that the velocity decay was steeper for reacting 1384
cases compared to non-reacting cases. 1385

The results presented in Figure FIXME however, show that even though Cases 1 1386
and 2 have similar Re , their mean velocity profiles have very different slopes. Further, 1387
the reacting and non-reacting cases (both at preheated conditions) have similarly 1388
steep slopes. This indicates that the mean axial stretch in the near field of the LSB 1389
flow field is a stronger function of the preheat temperature than Re . The presence 1390
of preheat results in increased viscosity that enhances the momentum transport in 1391
the radial direction. This causes the velocity decay to be steep for preheated cases, 1392
compared to cases without preheat. 1393

Assuming that S_T is constant, these results suggest that at higher preheat tem- 1394
peratures, the flame would stabilize closer to the dump plane because of the faster 1395
velocity decay and reduced local flow velocities. In fact, a faster velocity decay would 1396
produce greater u' values and increase S_T , further causing the flame location to shift 1397
upstream. Furthermore, in view of the steep velocity profile, it may be anticipated 1398
that any changes in the stabilization location caused by perturbations in the local 1399
flow field (and hence, the local turbulent flame propagation velocity) are likely to be 1400
of diminished magnitude in the presence of preheat. All of this leads to an intuitive 1401
result — the LSB flame behaves more stably at high preheat conditions. 1402

5.3 Effect of Swirler Vane Angle

1403

As described in Chapter 3, the LSB swirlers tested for this study are designed to have 1404
the same mass flow splits. The S_{45° swirler has a higher vane angle, resulting in greater 1405
blockage to the flow passing through the annular section. In order to compensate for 1406
this, the perforated plate covering the central section has slightly smaller holes. The 1407
net effect retains the same mass flow split as in the S_{37° swirler. 1408

Chapter 2 describes how the swirler vane angle relates to the amount of swirl im- 1409
parted to the incoming flow. According to Equation FIXME, a swirler with a higher 1410
vane angle will produce greater swirl in the reactants. Previous work in swirl com- 1411
bustion[19, 59] has pointed out that increased swirl shortens the flame by enhancing 1412
the swirl-induced radial pressure gradients. The data acquired in the present investi- 1413
gation is in agreement with this observation. Operated at identical inlet conditions, 1414
the S_{45° swirler stabilizes a flame closer to the dump plane and with a larger flame 1415
angle compared to the S_{37° swirler. 1416

This result highlights an interesting trade-off for the designers of LSB-based gas 1417
turbine engines. The S_{45° flame is located further upstream and has a more concen- 1418
trated region of heat release. This enhances the strength of the toroidal recirculation 1419
zone near the dump plane, which may be powerful enough under certain conditions 1420
(as we shall see in Section 5.4) to even cause the flame to attach itself to the lip of 1421
the inlet. All of this means that the S_{45° flame is more stable and will resist pertur- 1422
bations in the incoming flow better than the S_{37° flame. However, the presence of 1423
a strong recirculation zone in the flow field of the S_{45° swirler will entrain more hot 1424
products and retain them longer near the zone of heat release. This is a recipe for 1425
the production of thermal NO_x . While no emission measurements were made as part 1426
of this study, it may be reasonably anticipated that the NO_x performance of the S_{45° 1427
swirler will be degraded compared to the S_{37° swirler. The trade-off for gas turbine 1428

engine designers is thus between flame stability and emissions performance.

5.4 Effect of Equivalence Ratio

The LSB is primarily intended for fuel-lean operation in order to utilize its low NO_x emission performance. As a result, most of the testing was done as close as possible to a target ϕ of 0.56. Limited testing was carried out at 12 atm for two off-target conditions: a slightly richer ($\phi \approx 0.58$) and a slightly leaner ($\phi \approx 0.53$) mixture, in order to explore the sensitivity of the LSB flame to limited changes in equivalence ratio. The S_{45° swirler was used for these tests. The corresponding averaged and Abel-deconvoluted flame images are presented in Figure FIXME.

Two characteristics of the flame are immediately obvious from these images. First, the zone of heat release, marked by the region from which CH^* chemiluminescence is observed, is increasingly compact at fuel-rich conditions. Virtually all other flame images acquired at a leaner condition show a long flame, with the heat release distributed over the entire visible area of the combustor. The compactness of the heat release zone indicates potentially poor NO_x performance at these conditions.

Second, the fuel-rich flame brush can be observed to wrap around and anchor itself on the dump plane. This is particularly observable in the Abel-deconvoluted image. The attached region is not as bright as the rest of the flame brush, indicating that the flame may be attaching itself intermittently. This intermittent behavior can be confirmed from the instantaneous images where it is visible on some of the acquired images, but not others. This behavior was alluded to in Section 5.3 as being the result of the enhanced toroidal recirculation zone produced by this swirler. Thus, the intermittent attachment of the flame to the inlet indicates the increased importance of the toroidal recirculation zone in stabilizing the flame.

It should be noted that the reliance on a toroidal recirculation zone to anchor the flame to the inlet is one of the primary flame stabilization mechanisms used by

traditional swirl combustors. Thus, LSB swirlers with high vane angles tend to behave
like traditional swirl combustors at fuel-rich conditions.

5.5 Effect of Combustor Pressure

In many gas turbine engines, the combustor pressure varies directly with the loading
of the engine. Like the preheat temperature, the combustor pressure affects the LSB
flame both through the fluid mechanics of the flow and the kinetics of the chemical
reactions in the flame. The effect of the combustor pressure on the fluid mechanics
of the LSB flow field can be captured by its effect on the Reynolds number. As noted
in Section 5.2, however, previous work indicated the Reynolds number may not be
an important parameter for the LSB, particularly in the near field where the flame
stabilization occurs. On the other hand, the effect of the combustor pressure on reac-
tion rates in the flame is clearly important. Increasing the combustor pressure results
in a lower laminar flame speed and reduced flame thickness for methane-air flames.
According to the modified Damköhler model discussed earlier, the reduced laminar
flame speed should have little or no effect on the flow field, since the contribution from
 S_L in Equation 5.1 is vanishingly small, even at the lowest reference velocities
of our test conditions. However, as suggested by our discussion in Section 5.1, the
validity of the simple model at elevated pressure conditions is questionable.

In order to resolve the uncertainties regarding how the LSB flame responds to
combustor pressure, the flame was imaged over a range of operating conditions from
3 to 12 atm. For these tests, the reference velocity and the equivalence ratio were
held constant. However, the temperature of the reactants continues to increase with
pressure. The reason for this was discussed in Chapter 3 and is attributable to the
reduced heat losses in the connecting pipes at the high flow rates required to pressurize
the LSB. The flame location and shape inferred from the flame images are presented
in Figure 5.10.

At low to moderate pressures, the flame location is nearly invariant for S_{37° , but 1481
moves upstream for the S_{45° cases. This behavior can be explained as follows. The 1482
flame stabilization location for the S_{45° swirler is closer to the dump plane compared 1483
to the S_{37° swirler. This should result in enhanced heat transfer to the dump plane 1484
and consequently to the incoming reactants. This feedback is even more effective as 1485
the temperature of the incoming reactants increases. This causes the upstream shift 1486
of the S_{45° flame, while the S_{37° flame is less affected by these processes. 1487

At high pressures, however, both flames are observed to move downstream, despite 1488
the increasing preheat temperatures. The apparent decrease in the turbulent flame 1489
speed at these conditions is an unexpected result, and the modified Damköhler model 1490
is insufficient in accounting for this observation. Figure FIXME also shows that the 1491
flame angle for both cases decreases slightly with pressure. This suggests that the 1492
turbulent flame speed was consistently decreasing with pressure. In light of this, 1493
the nearly constant location of the S_{37° flame could be attributed to the effects of 1494
increasing combustor pressure and preheat temperature nearly canceling each other 1495
out at the lower pressures. 1496

5.6 Flame Structure 1497

CHAPTER 6
CONCLUSIONS

1498

1499

APPENDIX A

1500

SEEDER DESIGN

1501

A new seeder was designed for use in high pressure implementations of diagnostic techniques like Laser Doppler Velocimetry (LDV), Particle Image Velocimetry (PIV), etc.

1504

The previous design, as shown in Figure A.1, was a fluidized bed seeding generator. Seeding particles in a cylindrical vessel are fluidized by an air-turbine vibrator. Air is introduced into the vessel in the form of two opposing jets directed tangentially to produce a small amount of swirl in the flow field. Particles are picked up by the air flow and the swirl aids in separating the heavy/coagulated clumps of seeding particles by centrifugal acceleration.

1510

This design had several shortcomings. First, it is observed that the seeding density of the seeded flow generally decreases over time, even if the seeding particles have not been depleted. The seeding particles tend to coagulate over time, due to the buildup of moisture, static charge, etc. In such cases, the vibrator can no longer effectively fluidize the particles. Further, the tangential introduction of the air flow preferentially depletes particles near the walls of the container, leaving the center relatively undisturbed. The cumulative effect of these phenomena diminishes the effectiveness of the seeder.

1518

Second, the fluidized bed requires a minimum amount of seeding particles to function effectively. This requires the seeder to be refilled even before all the seeding particles are consumed.

1521

Third, when designed for high pressure applications, the seeder will become quite heavy due to flanges and other fittings. Such a setup cannot be easily fluidized using a reasonable-sized air-turbine vibrator.

1524

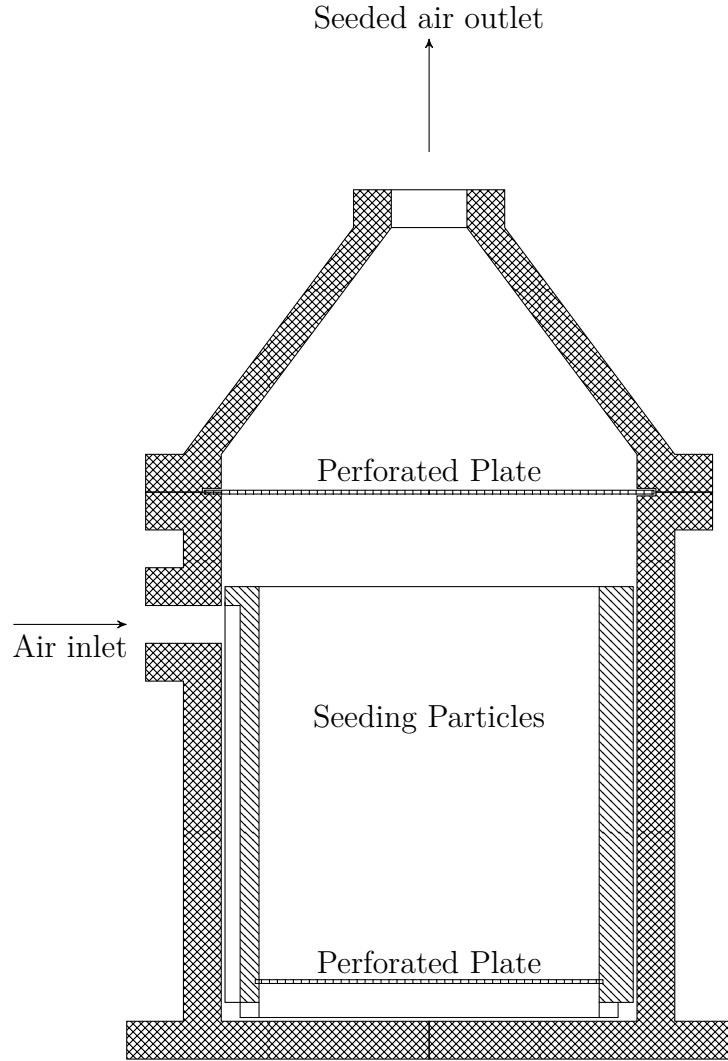


Figure A.1: A schematic of the old fluidized bed seeder is presented. The air enters the seeder through a groove along the inner vessel and is injected with a tangential velocity at the base of the seeder. The whole assembly is vibrated (vibrator not shown) to keep the particle bed fluidized. The seeded air flow exits through the outlet on the top.

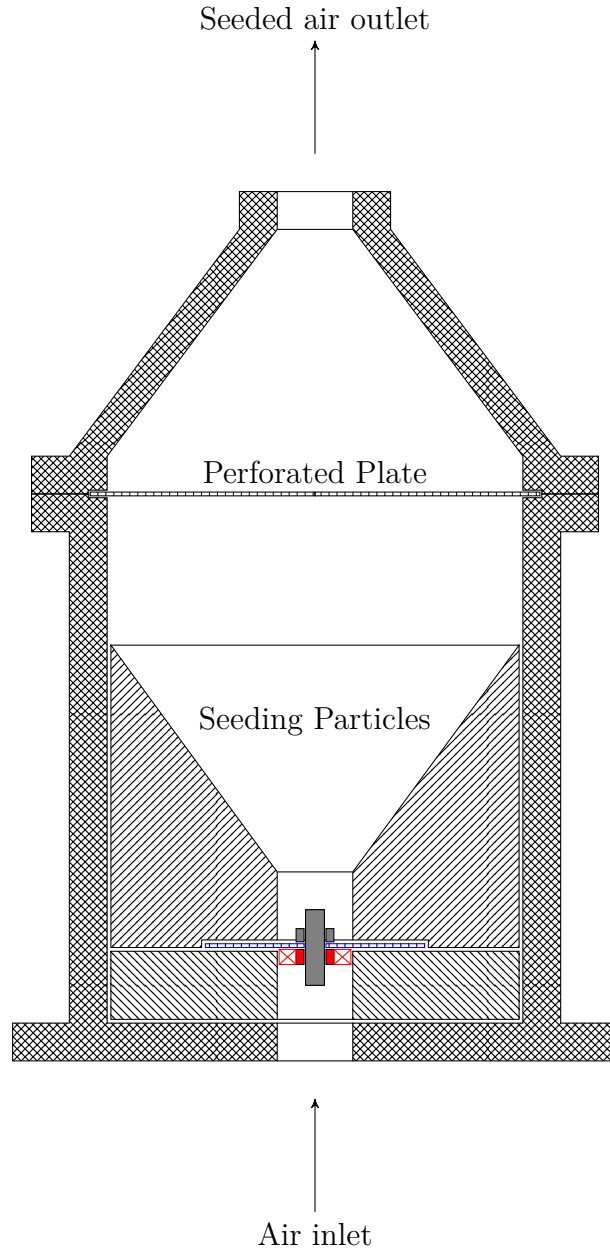


Figure A.2: *The improved design of the seeder is shown here in schematic form. The air enters the assembly from the inlet at the bottom, passes through the swirler (shown in red) and enters the seeder. The perforated plate at the bottom (shown in blue) keeps the seeding particles within the seeder. The swirler hub is threaded, allowing it to be secured to the perforated plate by a short steel bolt (shown in gray). After picking up the particles, a second perforated plate prevents large clumped seeding particles from passing through. The seeded air flow exits through the outlet at the top.*

The new seeder design is shown in Figure A.2, and resembles a funnel with a 1525
swirler located halfway up the stem. A perforated base plate holds the swirler and 1526
the seeding particles in the conical section of the swirler. Due to the steep angle of the 1527
sides of the conical section, the seeding particles continuously collapse into the central 1528
section. This negates any need for vibrating the system. Air is introduced from the 1529
bottom of the seeder and enters the vessel by passing through the swirler. Since all 1530
the air enters this way, there is a considerable amount of swirl in the resulting flow 1531
field, Heavy/coagulated seeding particles are flung outward, while lighter particles are 1532
carried with the air. After a sufficient distance to allow for the cyclonic separation 1533
to be effective, the seeded air passes through another perforated plate which further 1534
limits the presence of large clumps of particles. The exiting air is now spatially and 1535
temporally uniformly seeded. 1536

REFERENCES

1537

- [1] I. Glassman, *Combustion*. Academic Press, 1996. 1538
- [2] N. Syred and J. M. Beér, “Combustion in Swirling Flows: A Review,” *Combustion and Flame*, vol. 23, no. 2, pp. 143–201, 1974. 1539
1540
- [3] D. G. Lilley, “Swirl Flows in Combustion: A Review,” *AIAA Journal*, vol. 15, no. 8, pp. 1063–1078, 1977. 1541
1542
- [4] B. Bédard and R. K. Cheng, “Experimental Study of Premixed Flames in Intense Isotropic Turbulence,” *Combustion and Flame*, vol. 100, no. 3, pp. 485–494, 1995. 1543
1544
- [5] R. S. Barlow, R. W. Dibble, J. Y. Chen, and R. P. Lucht, “Effect of Damköhler Number on Superequilibrium OH Concentration in Turbulent Nonpremixed Jet Flames,” *Combustion and Flame*, vol. 82, no. 3-4, pp. 235–251, 1990. 1545
1546
1547
- [6] C. F. Kaminski, J. Hult, and M. Aldén, “High repetition rate planar laser induced fluorescence of OH in a turbulent non-premixed flame,” *Applied Physics B: Lasers and Optics*, vol. 68, no. 4, pp. 757–760, 1999. 1548
1549
1550
- [7] J. Hult, U. Meier, W. Meier, A. Harvey, and C. F. Kaminski, “Experimental analysis of local flame extinction in a turbulent jet diffusion flame by high repetition 2-D laser techniques and multi-scalar measurements,” in *Proceedings of the Combustion Institute*, vol. 30, pp. 701–709, 2005. 1551
1552
1553
1554
- [8] H. Malm, G. Sparr, J. Hult, and C. F. Kaminski, “Nonlinear diffusion filtering of images obtained by planar laser-induced fluorescence spectroscopy,” *Journal of The Optical Society of America A: Optics, image science, and vision*, vol. 17, no. 12, pp. 2148–2156, 2000. 1555
1556
1557
1558

- [9] R. Abu-Gharbieh, G. Hamarneh, T. Gustavsson, and C. F. Kaminski, “Flame front tracking by laser induced fluorescence spectroscopy and advanced image analysis,” *Optics Express*, vol. 8, no. 5, pp. 278–287, 2001.
- [10] C. M. Vagelopoulos and J. H. Frank, “An experimental and numerical study on the adequacy of CH as a flame marker in premixed methane flames,” in *Proceedings of the Combustion Institute*, vol. 30, pp. 241–249, 2005.
- [11] M. Köhler, A. Brockhinke, M. Braun-Unkhoff, and K. Kohse-Höinghaus, “Quantitative Laser Diagnostic and Modeling Study of C₂ and CH Chemistry in Combustion,” *The Journal of Physical Chemistry A*, vol. 114, no. 14, pp. 4719–4734, 2010.
- [12] C. P. Fenimore, “Formation of nitric oxide in premixed hydrocarbon flames,” in *Symposium (International) on Combustion*, vol. 13, pp. 373–380, 1971.
- [13] Z. S. Li, J. Kiefer, J. Zetterberg, M. Linvin, A. Leipertz, X. S. Bai, and M. Aldén, “Development of improved PLIF CH detection using an Alexandrite laser for single-shot investigation of turbulent and lean flames,” in *Proceedings of the Combustion Institute*, vol. 31, pp. 727–735, 2007.
- [14] H. N. Najm, P. H. Paul, C. J. Mueller, and P. S. Wyckoff, “On the Adequacy of Certain Experimental Observables as Measurements of Flame Burning Rate,” *Combustion and Flame*, vol. 113, no. 3, pp. 312–332, 1998.
- [15] J. Kiefer, Z. S. Li, J. Zetterberg, X. S. Bai, and M. Aldén, “Investigation of local flame structures and statistics in partially premixed turbulent jet flames using simultaneous single-shot CH and OH planar laser-induced fluorescence imaging,” *Combustion and Flame*, vol. 154, no. 4, pp. 802–818, 2008.

- [16] P. H. Paul and H. N. Najm, “Planar laser-induced fluorescence imaging of flame
heat release rate,” in *Symposium (International) on Combustion*, vol. 27, pp. 43–
50, 1998.
- [17] B. O. Ayoola, R. Balachandran, J. H. Frank, E. Mastorakos, and C. F. Kamin-
ski, “Spatially resolved heat release rate measurements in turbulent premixed
flames,” *Combustion and Flame*, vol. 144, no. 1, pp. 1–16, 2006.
- [18] J. Kiefer, Z. S. Li, T. Seeger, A. Leipertz, and M. Aldén, “Planar laser-induced
fluorescence of HCO for instantaneous flame front imaging in hydrocarbon
flames,” in *Proceedings of the Combustion Institute*, vol. 32, pp. 921–928, 2009.
- [19] C. K. Chan, K. S. Lau, W. K. Chin, and R. K. Cheng, “Freely propagating open
premixed turbulent flames stabilized by swirl,” in *Symposium (International) on
Combustion*, vol. 24, pp. 511–518, 1992.
- [20] R. K. Cheng, “Velocity and Scalar Characteristics of Premixed Turbulent Flames
Stabilized by Weak Swirl,” *Combustion and Flame*, vol. 101, no. 1-2, pp. 1–14,
1995.
- [21] T. Plessing, C. Kortschik, N. Peters, M. S. Mansour, and R. K. Cheng, “Measure-
ments of the turbulent burning velocity and the structure of premixed flames on
a low-swirl burner,” in *Proceedings of the Combustion Institute*, vol. 28, pp. 359–
366, 2000.
- [22] I. G. Shepherd and R. K. Cheng, “The Burning Rate of Premixed Flames in
Moderate and Intense Turbulence,” *Combustion and Flame*, vol. 127, no. 3,
pp. 2066–2075, 2001.
- [23] R. K. Cheng, I. G. Shepherd, B. Bédard, and L. Talbot, “Premixed turbulent flame
structures in moderate and intense isotropic turbulence,” *Combustion Science
and Technology*, vol. 174, no. 1, pp. 29–59, 2002.

- [24] I. G. Shepherd, R. K. Cheng, T. Plessing, C. Kortschik, and N. Peters, “Premixed flame front structure in intense turbulence,” in *Proceedings of the Combustion Institute*, vol. 29, pp. 1833–1840, 2002.
- [25] C. Kortschik, T. Plessing, and N. Peters, “Laser optical investigation of turbulent transport of temperature ahead of the preheat zone in a premixed flame,” *Combustion and Flame*, vol. 136, no. 1-2, pp. 43–50, 2004.
- [26] L. P. H. de Goey, T. Plessing, R. T. E. Hermanns, and N. Peters, “Analysis of the flame thickness of turbulent flamelets in the thin reaction zones regime,” in *Proceedings of the Combustion Institute*, vol. 30, pp. 859–866, 2005.
- [27] J. B. Bell, R. K. Cheng, M. S. Day, and I. G. Shepherd, “Numerical simulation of Lewis number effects on lean premixed turbulent flames,” in *Proceedings of the Combustion Institute*, vol. 31, pp. 1309–1317, 2007.
- [28] D. T. Yegian and R. K. Cheng, “Development of a lean premixed low-swirl burner for low NO_x practical applications,” *Combustion Science and Technology*, vol. 139, no. 1, pp. 207–227, 1998.
- [29] R. K. Cheng, D. T. Yegian, M. M. Miyasato, G. S. Samuelsen, C. E. Benson, R. Pellizzari, and P. Loftus, “Scaling and development of low-swirl burners for low-emission furnaces and boilers,” in *Proceedings of the Combustion Institute*, vol. 28, pp. 1305–1313, 2000.
- [30] D. Littlejohn, A. J. Majeski, S. Tonse, C. Castaldini, and R. K. Cheng, “Laboratory investigation of an ultralow NO_x premixed combustion concept for industrial boilers,” in *Proceedings of the Combustion Institute*, vol. 29, pp. 1115–1121, 2002.
- [31] M. R. Johnson, D. Littlejohn, W. A. Nazeer, K. O. Smith, and R. K. Cheng, “A comparison of the flowfields and emissions of high-swirl injectors and low-

- swirl injectors for lean premixed gas turbines,” in *Proceedings of the Combustion Institute*, vol. 30, pp. 2867–2874, 2005.
- [32] W. A. Nazeer, K. O. Smith, P. Sheppard, R. K. Cheng, and D. Littlejohn, “Full scale testing of a low swirl fuel injector concept for ultra-low NO_x gas turbine combustion systems,” in *Proceedings of ASME Turbo Expo GT2006-90150*, 2006.
- [33] R. K. Cheng, D. Littlejohn, W. A. Nazeer, and K. O. Smith, “Laboratory studies of the flow field characteristics of low-swirl injectors for adaptation to fuel-flexible turbines,” in *Proceedings of ASME Turbo Expo GT2006-90878*, 2006.
- [34] R. K. Cheng, D. Littlejohn, W. A. Nazeer, and K. O. Smith, “Laboratory Studies of the Flow Field Characteristics of Low-Swirl Injectors for Adaptation to Fuel-Flexible Turbines,” *Journal of Engineering for Gas Turbines and Power*, vol. 130, p. 021501, 2008.
- [35] R. K. Cheng and D. Littlejohn, “Effects of combustor geometry on the flowfields and flame properties of a low-swirl injector,” in *Proceedings of ASME Turbo Expo GT2008-50504*, 2008.
- [36] R. K. Cheng and D. Littlejohn, “Laboratory Study of Premixed H₂-Air and H₂-N₂-Air Flames in a Low-Swirl Injector for Ultralow Emissions Gas Turbines,” *Journal of Engineering for Gas Turbines and Power*, vol. 130, p. 031503, 2008.
- [37] D. Littlejohn and R. K. Cheng, “Fuel effects on a low-swirl injector for lean premixed gas turbines,” in *Proceedings of the Combustion Institute*, vol. 31, pp. 3155–3162, 2007.
- [38] R. K. Cheng, D. Littlejohn, P. A. Strakey, and T. Sidwell, “Laboratory investigations of a low-swirl injector with H₂ and CH₄ at gas turbine conditions,” in *Proceedings of the Combustion Institute*, vol. 32, pp. 3001–3009, 2009.

- [39] D. Littlejohn, R. K. Cheng, D. R. Noble, and T. Lieuwen, “Laboratory Investiga- 1655
tions of Low-Swirl Injectors Operating With Syngases,” *Journal of Engineering* 1656
for Gas Turbines and Power, vol. 132, p. 011502, 2010. 1657
- [40] P. Petersson, J. Olofsson, C. Brackman, H. Seyfried, J. Zetterberg, M. Richter, 1658
M. Aldén, M. A. Linne, R. K. Cheng, A. Nauert, D. Geyer, and A. Dreizler, 1659
“Simultaneous PIV/OH-PLIF, Rayleigh thermometry/OH-PLIF and stereo PIV 1660
measurements in a low-swirl flame,” *Applied Optics*, vol. 46, no. 19, pp. 3928– 1661
3936, 2007. 1662
- [41] R. H. Barnes, C. E. Moeller, J. F. Kircher, and C. M. Verber, “Dye-Laser Excited 1663
CH Flame Fluorescence,” *Applied Optics*, vol. 12, no. 11, pp. 2531–2532, 1973. 1664
- [42] J. F. Verdieck and P. A. Bonczyk, “Laser-induced saturated fluorescence in- 1665
vestigations of CH, CN and NO in flames,” in *Symposium (International) on* 1666
Combustion, vol. 18, pp. 1559–1566, 1981. 1667
- [43] M. G. Allen, R. D. Howe, and R. K. Hanson, “Digital imaging of reaction zones 1668
in hydrocarbon-air flames using planar laser-induced fluorescence of CH and C₂,” 1669
Optics Letters, vol. 11, no. 3, pp. 126–128, 1986. 1670
- [44] M. Namazian, R. L. Schmitt, and M. B. Long, “Two-wavelength single laser CH 1671
and CH₄ imaging in a lifted turbulent diffusion flame,” *Applied Optics*, vol. 27, 1672
no. 17, pp. 3597–3600, 1986. 1673
- [45] R. W. Schefer, M. Namazian, and J. Kelly, “Stabilization of lifted turbulent-jet 1674
flames,” *Combustion and Flame*, vol. 99, no. 1, pp. 75–86, 1994. 1675
- [46] P. H. Paul and J. E. Dec, “Imaging of reaction zones in hydrocarbon-air flames 1676
by use of planar laser-induced fluorescence of CH,” *Optics Letters*, vol. 19, no. 13, 1677
pp. 998–1000, 1994. 1678

- [47] C. D. Carter, J. M. Donbar, and J. F. Driscoll, “Simultaneous CH planar laser-
induced fluorescence and particle imaging velocimetry in turbulent nonpremixed
flames,” *Applied Physics B: Lasers and Optics*, vol. 66, no. 1, pp. 129–132, 1998.
- [48] K. A. Watson, K. M. Lyons, J. M. Donbar, and C. D. Carter, “Observations
on the Leading Edge in Lifted Flame Stabilization,” *Combustion and Flame*,
vol. 119, no. 1-2, pp. 199–202, 1999.
- [49] K. A. Watson, K. M. Lyons, J. M. Donbar, and C. D. Carter, “Simultaneous
Rayleigh Imaging and CH-PLIF Measurements in a Lifted Jet Diffusion Flame,”
Combustion and Flame, vol. 123, no. 1–2, pp. 252–265, 2000.
- [50] J. M. Donbar, J. F. Driscoll, and C. D. Carter, “Reaction Zone Structure in
Turbulent Nonpremixed Jet Flames—From CH-OH PLIF Images,” *Combustion
and Flame*, vol. 122, no. 1-2, pp. 1–19, 2000.
- [51] D. Han and M. G. Mungal, “Simultaneous measurement of velocity and CH layer
distribution in turbulent non-premixed flames,” in *Proceedings of the Combustion
Institute*, vol. 28, pp. 261–267, 2000.
- [52] P. S. Kothnur, M. S. Tsurikov, N. T. Clemens, J. M. Donbar, and C. D. Carter,
“Planar imaging of CH, OH, and velocity in turbulent non-premixed jet flames,”
in *Proceedings of the Combustion Institute*, vol. 29, pp. 1921–1927, 2002.
- [53] D. Han and M. G. Mungal, “Simultaneous measurements of velocity and CH
distributions. Part 1: jet flames in co-flow,” *Combustion and Flame*, vol. 132,
no. 3, pp. 565–590, 2003.
- [54] D. Han and M. G. Mungal, “Simultaneous measurements of velocity and CH
distributions. Part II: deflected jet flames,” *Combustion and Flame*, vol. 133,
no. 1–2, pp. 1–17, 2003.

- [55] J. A. Sutton and J. F. Driscoll, “Optimization of CH fluorescence diagnostics
in flames: range of applicability and improvements with hydrogen addition,”
Applied Optics, vol. 42, no. 15, pp. 2819–2828, 2003.
- [56] Z. S. Li, J. Zetterberg, M. Linvin, M. Aldén, J. Kiefer, T. Seeger, and A. Leipertz,
“Planar laser-induced fluorescence of combustion intermediates in turbulent
methane/air flames stabilized on a co-axial jet flame burner,” in *Proceedings
of the European Combustion Meeting, ECM2007, Chania, Crete, Greece*, vol. 3,
pp. 5–12–1–6, 2007.
- [57] J. Kiefer, Z. Li, J. Zetterberg, M. Linvin, and M. Aldén, “Simultaneous laser-
induced fluorescence and sub-Doppler polarization spectroscopy of the CH radi-
cal,” *Optics Communications*, vol. 270, no. 2, pp. 347–352, 2007.
- [58] Z. S. Li, M. Afzelius, J. Zetterberg, and M. Aldén, “Applications of a single-
longitudinal-mode alexandrite laser for diagnostics of parameters of combustion
interest,” *Review of Scientific Instruments*, vol. 75, no. 10, pp. 3208–3215, 2004.
- [59] S. H. Stårner and R. W. Bilger, “Joint measurements of velocity and scalars in
turbulent diffusion flame with moderate swirl,” in *Symposium (International) on
Combustion*, vol. 21, pp. 1569–1577, 1986.
- [60] H. Kobayashi, Y. Kawabata, and K. Maruta, “Experimental study on general
correlation of turbulent burning velocity at high pressure,” in *Symposium (In-
ternational) on Combustion*, vol. 27, pp. 941–948, 1998.
- [61] H. Kobayashi, “Experimental study of high-pressure turbulent premixed flames,”
Experimental Thermal and Fluid Science, vol. 26, no. 2, pp. 375–387, 2002.
- [62] P. Griebel, P. Siewert, and P. Jansohn, “Flame characteristics of turbulent lean
premixed methane/air flames at high pressure: Turbulent flame speed and flame

- brush thickness,” in *Proceedings of the Combustion Institute*, vol. 31, pp. 3083– 1727
3090, 2007. 1728
- [63] H. Kobayashi, T. Nakashima, T. Tamura, K. Maruta, and T. Niioka, “Turbu- 1729
lence Measurements and Observations of Turbulent Premixed Flames at Elevated 1730
Pressures up to 3.0 MPa,” *Combustion and Flame*, vol. 108, no. 1-2, pp. 104–117, 1731
1997. 1732
- [64] A. C. Eckbreth, *Laser diagnostics for combustion temperature and species*. CRC, 1733
1996. 1734
- [65] J. W. Daily, “Laser induced fluorescence spectroscopy in flames,” *Progress in* 1735
Energy and Combustion Science, vol. 23, no. 2, pp. 133–199, 1997. 1736
- [66] J. Luque and D. R. Crosley, “Electronic transition moment and rotational transi- 1737
tion probabilities in CH. II. $B^2\Sigma^- - X^2\Pi$ system,” *Journal of Chemical Physics*, 1738
vol. 104, no. 11, pp. 3907–3913, 1996. 1739
- [67] N. L. Garland and D. R. Crosley, “Energy transfer processes in CH $A^2\Delta$ 1740
and $B^2\Sigma^-$ in an atmospheric pressure flame,” *Applied Optics*, vol. 24, no. 23, 1741
pp. 4229–4237, 1985. 1742
- [68] G. Richmond, M. L. Costen, and K. G. McKendrick, “Collision-Partner Depen- 1743
dence of Energy Transfer between the CH $A^2\Delta$ and $B^2\Sigma^-$ States,” *The Journal* 1744
of Physical Chemistry A, vol. 109, no. 4, pp. 542–553, 2005. 1745
- [69] E. F. van Dischoeck, “Photodissociation processes in the CH molecule,” *The* 1746
Journal of Chemical Physics, vol. 86, no. 1, pp. 196–214, 1987. 1747
- [70] J. Luque, R. J. H. Klein-Douwel, J. B. Jeffries, and D. R. Crosley, “Collisional 1748
processes near the CH $B^2\Sigma^- v' = 0, 1$ predissociation limit in laser-induced fluo- 1749

- rescence flame diagnostics,” *Applied Physics B: Lasers and Optics*, vol. 71, no. 1, pp. 85–94, 2000.
- [71] J. Luque and D. R. Crosley, “Electronic transition moment and rotational transition probabilities in CH. I. $A^2\Delta - X^2\Pi$ system,” *Journal of Chemical Physics*, vol. 104, no. 6, pp. 2146–2155, 1996.
- [72] A. Marshall, P. Venkateswaran, D. Noble, J. Seitzman, and T. Lieuwen, “Development and characterization of a variable turbulence generation system,” *Experiments in Fluids*, vol. 51, no. 3, pp. 611–620, 2011.
- [73] A. Melling, “Tracer particles and seeding for particle image velocimetry,” *Measurement Science and Technology*, vol. 8, no. 1, pp. 1406–1416, 1997.
- [74] B. Hemmerling, “Beam steering effects in turbulent high-pressure flames,” in *Proceedings of SPIE*, vol. 3108, pp. 32–37, 1997.
- [75] C. J. Dasch, “One-dimensional tomography: a comparison of abel, onion-peeling, and filtered backprojection methods,” *Applied Optics*, vol. 31, no. 8, pp. 1146–1152, 1992.
- [76] N. L. Garland and D. R. Crosley, “Relative transition probability measurements in the $A - X$ and $B - X$ systems of CH,” *Journal of Quantitative Spectroscopy and Radiative Transfer*, vol. 33, no. 6, pp. 591–595, 1985.
- [77] M. Zachwieja, “New Investigations of the $A^2\Delta - X^2\Pi$ Band System in the CH Radical and a New Reduction of the Vibration-Rotation Spectrum of CH from the ATMOS Spectra,” *Journal of Molecular Spectroscopy*, vol. 170, no. 2, pp. 285–309, 1995.